# Aircraft In-situ Measurements from SOCRATES Constrain the Anthropogenic Perturbations of Cloud Droplet Number

Ci Song<sup>1</sup>, Daniel T. McCoy<sup>1</sup>, Isabel L. McCoy<sup>2, 3</sup>, Hunter Brown<sup>1</sup>, Andrew Gettelman<sup>4</sup>, Trude Eidhammer<sup>5</sup>, and Donifan Barahona<sup>6</sup>

Correspondence: Ci Song (csong@uwyo.edu)

Abstract. Aerosol-cloud interactions (ACI) in warm clouds alter reflected shortwave radiation by influencing cloud microphysical and macrophysical properties. The variable of state controlling ACI is the cloud droplet number concentration ( $N_d$ ). Here, we examine the perturbations in  $N_d$  due to anthropogenic aerosols ( $\Delta N_{d,PD-PI}$ ) using a perturbed parameter ensemble (PPE) hosted in the sixth Community Atmosphere Model (CAM6). Surrogate models are created for the CAM6 PPE outputs and are used to generate 1 million model variants of CAM6 by sampling 45 sources of parameter uncertainty. The range of uncertain physical parameters related to ACI are constrained with observations of aerosol and cloud properties from SOCRATES. The likely range of uncertain parameters and the associated range of  $\Delta N_{d,PD-PI}$  are more strongly constrained with observations of  $N_d$  relative to observations of cloud condensation nuclei. We conduct sensitivity tests of how constraints on  $\Delta N_{d,PD-PI}$  are affected by systematic uncertainties in observations and our limitations in our surrogate models created for CAM6 PPE outputs. Based on this, we provide guidance on the impact of reducing systematic uncertainty in airborne microphysical observations and in surrogate models.

#### 1 Introduction

Clouds play an essential role in setting Earth's top of atmosphere energy flux by reflecting incoming shortwave radiation back to space. Aerosols are important for cloud formation as they serve as cloud condensation nuclei (CCN) for water vapor to condense onto. CCN make cloud droplet formation possible in atmospheric conditions. Aerosols from anthropogenic emissions alter cloud droplet number concentration  $(N_d)$  by acting as CCN, enhancing cloud reflectivity (Twomey, 1977). The change in reflected shortwave radiation (i.e., radiative forcing: RF in W/m<sup>2</sup>) through changes in  $N_d$  is referred to as the instantaneous radiative forcing due to aerosol-cloud interactions (IRFaci). According to the formulation in Bellouin et al. (2020), IRFaci is given by

$$IRFaci = \frac{\partial R}{\partial \ln N_d} \bigg|_{LWP_c,C} \cdot \Delta \ln N_d \tag{1}$$

<sup>&</sup>lt;sup>1</sup>Department of Atmospheric Science, University of Wyoming, Laramie, WY, USA

<sup>&</sup>lt;sup>2</sup>Cooperative Institute for Research in Environmental Sciences, University of Colorado, Boulder, CO, USA

<sup>&</sup>lt;sup>3</sup>National Oceanic and Atmospheric Administration, Chemical Sciences Laboratory, Boulder, CO, USA

<sup>&</sup>lt;sup>4</sup>Pacific Northwest National Laboratory, Richland, WA, USA

<sup>&</sup>lt;sup>5</sup>NSF National Center for Atmospheric Research, Boulder, CO, USA

<sup>&</sup>lt;sup>6</sup>Global Modeling and Assimilation Office, NASA Goddard Space Flight Center, Greenbelt, MD, USA

where R is the net radiative flux.  $LWP_c$  is the in-cloud liquid water path (LWP) and  $\Delta lnN_d$  is the fractional perturbation in  $N_d$  (Ghan et al., 2016; Bellouin et al., 2020). The vertical line in the partial derivative denotes  $LWP_c$  and cloud fraction (C) are held constant (Bellouin et al., 2020). With changes in  $N_d$ , cloud macrophysical properties can be altered in response to changes in cloud microphysics, such as cloud lifetime, liquid water content and cloud cover (Ackerman et al., 2004). The RF caused by modifications to cloud macrophysics is referred to as aerosol-cloud adjustment and is given by

$$RF_{adjustment} = \left(\frac{\partial R}{\partial C} \frac{dC}{dlnN_d} + \frac{\partial R}{\partial LWP_c} \frac{dLWP_c}{dlnN_d}\right) \cdot \Delta lnN_d \tag{2}$$

The sum of radiative forcing from IRFaci and aerosol-cloud adjustment is termed effective RF due to ACI (ERFaci), which can be expressed as

$$ERFaci = \left(\left.\frac{\partial R}{\partial \ln N_d}\right|_{LWP_c} + \frac{\partial R}{\partial C} \cdot \frac{dC}{d\ln N_d} + \frac{\partial R}{\partial LWP_c} \cdot \frac{dLWP_c}{d\ln N_d}\right) \cdot \Delta \ln N_d \tag{3}$$

Recent assessments place ERFaci as the largest uncertainty in anthropogenic climate forcing. This uncertainty also complicates efforts to infer climate sensitivity from the historical record, as the cooling from ACI can mask the warming effects of greenhouse gases (GHGs) (Bellouin et al., 2020; Forster, 2016; Watson-Parris and Smith, 2022).

30

Earth system models (ESMs) are essential for estimating ERFaci as they can estimate the unobservable preindustrial baseline of the atmosphere (Carslaw et al., 2017; Wall et al., 2022). However, ESMs are uncertain in their representations of aerosols and their climate effects. This uncertainty can be related to structural uncertainty (what processes to include in a model) (Regayre et al., 2023) and parametric uncertainty (how the values of parameters in the mathematical representation of processes are set in the ESM) (Regayre et al., 2018). The uncertainties in ERFaci related to parametrizations of unresolved aerosol processes, emissions, and cloud microphysical processes within a single model can be as large as the spread across models with different model structures. This supports the utility of understanding parametric uncertainties (Johnson et al., 2018). A commonly used method is to employ a perturbed parameter ensemble (PPE). This method involves exploring many possible parameter combinations across their uncertainty range to quantify the range of possible outcomes. The plausible range of ERFaci can be estimated using a set of parameter combinations, provided there is good agreement between observations and the model simulations generated by those parameter combinations (Regayre et al., 2018).

Wood (2012) argues that the variable of state (or most important variable) in understanding ACI is the  $N_d$ . Effectively, changes in  $N_d$  play a pivotal role in governing cloud radiative and macrophysical behavior. This means that to reduce uncertainty in ERFaci, constraining the anthropogenic perturbation to  $N_d$  is essential as both IRFaci (Eq 1) and aerosol-cloud adjustment (Eq 2) scale with change in  $N_d$  (Bellouin et al., 2020; Song et al., 2024).

One obstacle in seeking an observational constraint on the  $N_d$  response to anthropogenic aerosol is that the processes driving the  $N_d$  response primarily occur at the microscale and the result of these processes poses observational challenges. Past studies have used observations of  $N_d$  from spaceborne remote sensing to constrain the change in  $N_d$  during historical periods, achieving consistent observational constraints across different host models using the same observations (McCoy et al., 2020; Song et al., 2024; Gryspeerdt et al., 2016). However, observations of aerosol and cloud microphysical properties from remote sensing are known to have uncertainties arising from factors such as assumptions about particle size distributions, cloud

microphysics, and radiative transfer models used in the retrieval process (Grosvenor et al., 2018; Zhang et al., 2016; Gryspeerdt et al., 2022).

In-situ measurements provide direct measurements of aerosol and cloud microphysical properties without reliance on retrieval algorithms or assumptions used in remote sensing. It also measures more detailed microphysical properties such as aerosol size distribution, chemical composition, and cloud droplet number concentration and size distributions. However, insitu measurements can suffer from a wide variety of instrument biases and limitations and the impact of these limitations on our ability to use them for climate studies is not well characterized. For instance, instruments used for measuring aerosol and cloud properties can only detect subsets of the full particle distribution due to their limited sampling volume, and they cannot measure the full spectrum of particle sizes (Lance et al., 2010). In-situ measurements from aircraft occur with a much smaller footprint than a typical ESM and are often targeted towards features that make them not representative to compare to an ESM grid cell (Field and Furtado, 2016). Additionally, by their nature aircraft campaigns have minimal global coverage and it is unclear how effective a constraint on global model behavior they provide.

In this paper, we focus on characterizing an observational constraint on the change in  $N_d$  during the historical period  $(\Delta N_{d,PD-PI})$  based on in-situ measurements from a single campaign to illustrate the utility of combining two key tools: ESMs and airborne observations of microscale properties. We expand on previous work (Gettelman et al., 2020) by examining parametric uncertainty across a single ESM (i.e. using a PPE) and characterizing what we can learn from an airborne campaign and expanding on previous PPE work leveraging surface observations of aerosol properties (Regayre et al., 2020). We use observations of both aerosol and cloud properties from aircraft in-situ measurements. We address the following question: 1) do aerosol or cloud measurements better constrain global cloud microphysical behavior? 2) can sparse in-situ measurements produce constraints on cloud microphysical behavior on a global scale? 3) how sensitive is the observational constraint on  $\Delta N_{d,PD-PI}$  to observation uncertainties? We provide this analysis with the goal of (i) showing the connection between insitu measurements and our understanding of climate (Regayre et al., 2020) and (ii) characterizing where to expend effort in terms of sampling with in-situ measurements and model development.

#### 2 Materials and Methods

80

# 75 2.1 The CAM6 Perturbed parameter ensemble

We use the Community Atmosphere Model version 6 (CAM6), which is the atmosphere component of the Community Earth System Model version CESM-2.0 (Danabasoglu et al., 2020). The CAM6 model uses a two-moment microphysics scheme for stratiform clouds, with liquid, ice, rain, and snow hydrometeors calculated as prognostic variables, allowing CAM6 to explicitly represent the aerosol indirect effect (Gettelman and Morrison, 2015; Gettelman et al., 2015).

We leverage a perturbed parameter ensemble (PPE) hosted in CAM6 (Eidhammer et al., 2024). A PPE is a large set of simulations based on the structure of a single ESM (e.g., CAM6) with a different combination of parameter values to examine parameter uncertainty (Lee et al., 2011; Carslaw et al., 2013). The CAM6 PPE is fully described in Eidhammer et al. (2024). CAM6 is run at the standard resolution of 1.25°×0.9375° resolution. Briefly, 262 model simulations (i.e., 262 parameter com-

binations) of CAM6 sample 45 sources of uncertainty in the parameterizations for cloud, precipitation, convection, boundary layer, and aerosol processes. The 45 parameters are simultaneously perturbed using Latin Hypercube within the plausible range of realistic values based on expert-elicitation. We examine 203 ensemble members out of 262 integrated. The remaining 59 members were excluded based on criterion: (1) the linear regression slope of  $N_d$  to CCN in log space  $(dlnN_d/dlnCCN)$  is less than 0; (2) the correlation coefficient between  $N_d$  and CCN is less than 0.3. The two criteria are used to exclude PPE members that are too far outside the observational constraint behaviors (i.e., the Southern Ocean field campaign measurements analyzed in Figure 14 in McCoy et al. (2021)). Following Song et al. (2024), we also exclude PPE members that simulate too much ice in tropics, which is inconsistent with satellite observations (King et al., 2013).

# 2.2 Model Configuration

100

105

110

115

Two scenarios are simulated and each of them use the same parameter combinations - consistent with previous studies (Song et al., 2024). First, 2-year global simulations saved at monthly-mean are completed for pre-industrial (PI) and present-day (PD) emissions. PI and PD aerosol emission scenarios are integrated from 2019 to 2020 so anthropogenic perturbations in  $N_d$  can be calculated over global coverage by taking the difference between PI and PD. The atmosphere is nudged to horizontal winds and temperature and sea surface temperature and sea ice fraction are prescribed from observations. Wind and temperature fields are nudged to the Modern-Era Retrospective analysis for Research and Applications, Version 2 (MERRA2) reanalysis (Bosilovich et al., 2015) with 24-hour relaxation time. MERRA2 output is interpolated to CAM6 vertical resolution with standard 32 vertical levels from the surface to 3 hPa following Gettelman et al. (2020). Previous studies have shown the CAM6 PPE produces a wide range of perturbations in cloud microphysics (e.g.,  $\Delta N_{d,PD-PI}$ ) and cloud macrophysics ( $\Delta LWP_{PD-PI}$ ). In this study, we focus on diagnosing the parametric effects on cloud microphysical responses to anthropogenic aerosols from different parameter combinations using the PPE.

In addition to the two-year integrations of the PPE used to calculate anthropogenic perturbations in  $N_d$ , the PPE is integrated over short periods consistent with the Southern Ocean Clouds, Radiation, Aerosol, Transport Experimental Study (SOCRATES) field campaign based from Hobart, Tasmania (McFarquhar et al., 2021) (Figure 1). The SOCRATES campaign occurred over the midlatitude Southern Ocean (SO) during austral summer and was dominated by a series of frontal systems, postfrontal stratocumulus decks, and cyclonic activity typical of the storm track region (McFarquhar et al., 2021). Model outputs are saved along flight tracks over SOCRATES and is sampled at 1 min resolution following Gettelman et al. (2020). It applies atmospheric nudging to horizontal winds and temperature, consistent with global simulation with PI and PD aerosol emissions scenarios, but nudged to the period of January-March 2018 when the aircraft observations were conducted. The behavior of the default parameter configuration in CAM6 has been characterized using this approach in Gettelman et al. (2020); McCoy et al. (2021); McCluskey et al. (2023); Zhou et al. (2021).

Previous studies have shown that the CAM6 PPE, configured with 2-year global simulations, produces a wide spread in present-day (PD) cloud microphysical ( $N_d$ ) and macrophysical (LWP) properties. The mean-state PD values have been shown to fall within the observational range derived from satellite remote sensing (Song et al., 2024). Additionally, CAM6 simulations along flight tracks using the default parameter configuration reproduce many features of in-situ observations, including cloud

phase, cloud location, and boundary layer structure (Gettelman et al., 2020). These results give us confidence that at least some members of the nudged PPE simulations provide a physically plausible baseline in terms of cloud microphysical and macrophysical properties. In this study, we focus specifically on microphysical properties.

#### 2.3 Aircraft Sampling

120

125

130

135

140

150

We examine in-situ airborne observations taken from SOCRATES as our observational constraint (McFarquhar et al., 2021). The importance of the Southern Ocean (SO) to understanding the global anthropogenic contribution to  $N_d$  has been shown in several previous studies (Carslaw et al., 2013; McCoy et al., 2020). The National Science Foundation Gulfstream-V (GV) aircraft was deployed during January-March 2018 for SOCRATES. There were 15 flights sampling data from 42°S to 62°S with aerosol and cloud properties sampled at 1 Hz frequency. The GV was equipped with a variety of sensors and instruments. In this work,  $N_d$  from the cloud droplet probe (CDP) and aerosol number concentrations from the ultra-high sensitivity aerosol spectrometer (UHSAS) are examined. We focus on accumulation mode aerosols, with diameters ranging from 0.1  $\mu$ m to 1  $\mu$ m, reported as UHSAS100 in this paper following McCoy et al. (2021). Accumulation mode aerosol usually accounts for most of the surface area of aerosols and is a good estimate of the CCN concentration for stratocumulus updraft velocities (Seinfeld and Pandis, 2016).

With a focus on low-level, liquid cloud, we restrict the aircraft measurements of aerosol and cloud to be below 2 km. As in previous studies (McCoy et al., 2021), in-situ aircraft aerosol measurements are discarded when the liquid water content (LWC) from the CDP exceeds 0.001  $\frac{g}{m^{-3}}g/m^3$ , along with the subsequent 10 seconds after cloud detection. This is to avoid measurement contamination from cloud (McCoy et al., 2021). In-cloud  $N_d$  measurements are restricted to regions where the LWC from the CDP is greater than a threshold  $(0.1 \frac{g/m^{-3}g/m^3})$  following McCoy et al. (2021). Because the observations of aerosols and in-cloud  $N_d$  that are considered valid for use are taken at different locations, direct comparison is challenging due to inconsistencies in spatial and temporal coverage. To make comparisons between  $N_d$  and aerosol observations, we bin the aircraft measurements by 2 min in duration and 50 m in altitude so that aerosols and  $N_d$  can be compared in the same bin. Only bins with at least ten 1 Hz flight observations are considered valid composites for use. Median values of aerosol concentration and  $N_d$  are computed for each bin for observations from each flight following McCoy et al. (2021). The instrument limitation inevitably forces us to look either at small clouds or cloud edges, where both the measurements of aerosol and cloud are valid for use. This has minimal impact on our comparison between models and observations as we colocate model output with observations as detailed in Section 2.4.

145 In this study, we focus exclusively on low-level, liquid clouds simulated by the stratiform (large-scale) cloud microphysics scheme (MG2) in CAM6, as CAM6's convective scheme does not include prognostic microphysical variables such as  $N_d$ , which is a key quantity in our analysis. As such, all  $N_d$  values analyzed in this study originate from the stratiform cloud scheme. Furthermore, we limit our comparison with aircraft observations to altitudes below 2 km, corresponding to the marine boundary layer and excluding a large potion of clouds formed by deep convection (Kang et al., 2024). The majority of simulated N<sub>d</sub> in CAM6 is also concentrated below 2 km (Zhou et al., 2021). The convective scheme, while it may be triggered during

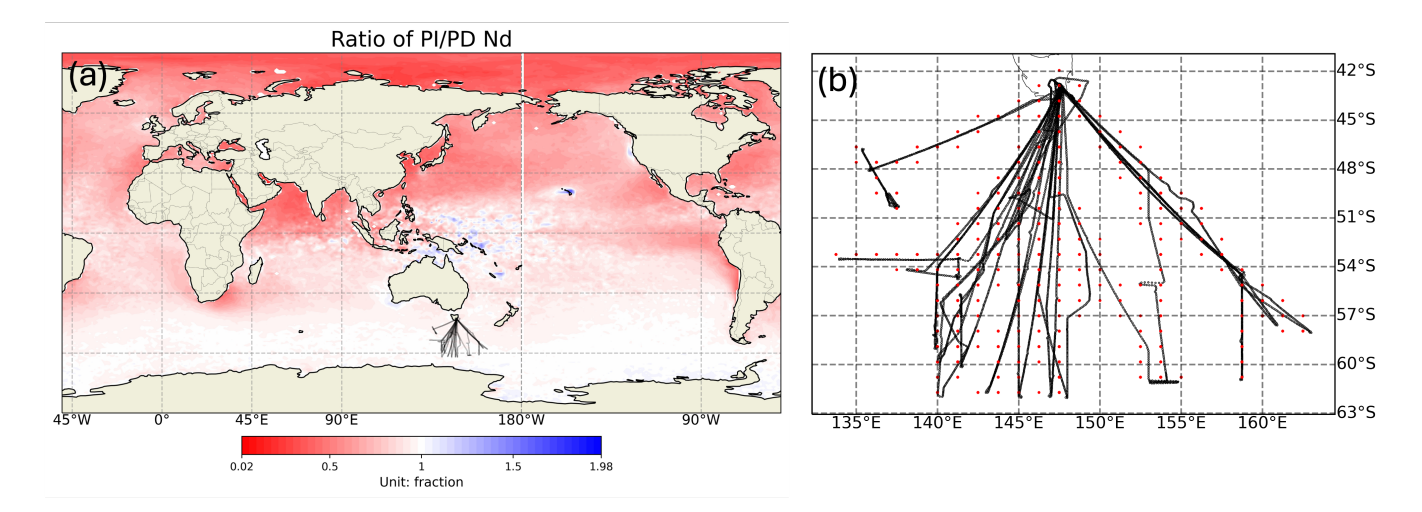


Figure 1. Maps of SOCRATES mission flight tracks from the NSF G-V aircraft. (a) Location of the SOCRATES aircraft sampling and the ratio of preindustrial to present day  $N_d$  shown in colors. The ratio is computed as  $\frac{PINd}{PDNd}$  using the preindustrial and present-day simulations run for two years configured with default CAM6 parameter setting. Ratios less than 1 indicate anthropogenically polluted regions. (b) Comparison of sampling of aircraft measurements (black line) with CAM6 grid point centers (red dots). Along-flight-track simulations are run for January–March 2018, covering late austral summer into early autumn.

postfrontal cloud conditions, does not contribute to  $N_d$  in CAM6. The convective scheme can contribute to precipitation, while this is beyond the scope of analysis in the present study.

#### 2.4 Comparison Between Model data and Observations

165

The default configuration of CAM6 has been extensively evaluated in Gettelman et al. (2020) and McCoy et al. (2021) and has been shown to be able to reproduce many features consistent with in-situ observations in Gettelman et al. (2020). Here, we examine a PPE that is hosted in the same model evaluated in previous studies (McCoy et al., 2021; Gettelman et al., 2020). The CAM6 model parameterization and the prior distribution of parameters (i.e., 217 sets of parameter combinations) in the PPE (Eidhammer et al., 2024) produce simulated aerosol and cloud properties that we can compare with observations to evaluate how process representation impacts aerosol-cloud interactions. Here, we focus on microphysical quantities that are available from in-situ measurements but hard to observe from spaceborne remote sensing.

 $N_d$  is directly available from both CAM6 and in-situ measurements from the CDP. CAM6 in-cloud  $N_d$  is calculated as  $N_d$  divided by liquid cloud fraction (when cloud fraction  $\leq 1\%$ , we set  $N_d = 0$ ). This cloud fraction threshold is smaller than the one used in McCoy et al. (2021) as we found it retains more flight composites but does not significantly change the results of our analysis (Figure S1).

CCN is a subset of aerosols that can be activated to cloud droplets at a given supersaturation. CAM6 outputs CCN at a set of fixed supersaturations. Here, we look at supersaturation at 0.2%. It is found that observed CCN at 0.2% supersaturation

(CCN02) has an one-to-one relationship with accumulation mode aerosol (e.g., UHSAS100) measured over SOCRATES (McCoy et al., 2021). Following previous work (McCoy et al., 2021), we use UHSAS100 as a proxy to CCN02 over SOCRATES as UHSAS100 lies very close to the one-to-one line with CCN02. This supersaturation level is shown to be representative of marine low-level stratocumulus (Hudson and Svensson, 1995).

To make comparisons between the modeled and observed  $N_d$  and aerosol properties, model data are colocated to observations by linearly interpolating to temporal and spatial locations from the 2 min  $\times$  50 m observational composites following McCoy et al. (2021). Our comparison between observations and models follows two strategies. First, model outputs (CCN and  $N_d$ ) are confronted with in-situ observations for collocated bins (flight track composites) along flight tracks for each simulation ensemble. This method allows for the evaluation of simulated CCN,  $N_d$ , and the inferred efficiency of aerosol activation ( $\frac{dNd}{dCCN}$ ) relative to observations within individual PPE members. The results are discussed in Section 3.1. Second, campaign-means of CCN and  $N_d$  are calculated for each PPE ensemble and compared with campaign-means of CCN and  $N_d$  calculated from in-situ observations. In this approach, we evaluate aerosol activation efficiency across the CAM6 PPE members (run with different parameter sets) and use campaign-means of in-situ aerosol properties and  $N_d$  to constrain the CAM6 PPE (Section 3.3.3).

The intention of taking the campaign-mean is to reduce random error by averaging over a large number of samples. However, there remains potential sources of systematic error. One possible source of systematic error is from differences in sampling between the observations and the model (e.g. if the pilot only flew through clear air and avoided cloud). Sampling during airborne campaigns may have some systematic sampling biases as discussed in Field and Furtado (2016). Output from CAM6 is representative of an average within the grid box of the model, whereas flight patterns in a similar-sized domain may not be sampling randomly (e.g. focusing on convective cores). We believe that this is a minimal concern for SOCRATES. The SOCRATES flight pattern was designed to focus on cold sectors of cyclones and synoptically uplifted aerosol layers, but followed a random sampling pattern in those large-scale features (McCoy et al., 2021). In addition to any systematic errors from sampling strategy, instrument error inherent in the CDP introduces additional uncertainties in the measurements of  $N_d$ . CDP measures cloud droplets within a specific size range (i.e., 2 to 50  $\mu$ m in diameter). It has limitations regarding droplets that fall outside its designed size range. Coincidence errors may occur when multiple droplets pass through the sensor's detection volume but is counted as a single droplet. The impact of observational uncertainty on the model constraints is examined in in section 3.4.

Another potential source of systematic uncertainty may arise from the use of UHSAS100 as a proxy to CCN02 over SOCRATES. While a near one-to-one relationship between UHSAS100 and CCN02 has been reported for the SOCRATES campaign (e.g., (McCoy et al., 2021))(McCoy et al., 2021), the campaign-mean ratio of CCN02 to UHSAS100 is approximately 1.08 (±0.3)according to , based on the median and interquartile range of the CCN02:UHSAS100 ratio uncertainty shown in their Figure S2. This suggests that UHSAS100 may underestimate CCN02 by 8% on average. Moreover, the activation diameter for SO aerosol is typically below 100 nm at 0.2% supersaturation, and likely closer to 80 nm for the aerosol population sampled during SOCRATES (Fossum et al., 2018; Mallet et al., 2025). This suggests that USHS100 may introduce an even greater underestimation of CCN02 compared to UHSAS100. To reflect the potential offset between UHSAS100 and

CCN02, we conducted sensitivity tests by increasing the observed "CCN" by 8% and 40%, representing the lower and upper bounds of the CCN02 to N100 ratio uncertainty, to examine how this affects our results (Section 3.3.3).

Having discussed uncertainty in the observations, we can turn our attention to uncertainty in the representation of processes in models. While the PPE samples a large number of possible representations of the underlying physics, it is still quite sparse (Lee et al., 2011). To systematically explore parametric uncertainty across the PPE, we build emulators (surrogate models) for the campaign-mean  $N_d$  and CCN using Gaussian Process (GP) regression (Watson-Parris et al., 2021). Emulators are trained by using the 45 perturbed parameters as inputs and simulation outputs (e.g., campaign-mean  $N_d$  and CCN) using a subset of the PPE ensemble as training data. Emulators are trained on the sample of different process representations in the CAM6 PPE data (Figure S2). The creation and validation of the emulators follows previous literature (Lee et al., 2011; Regayre et al., 2020; Song et al., 2024). With the GP emulators, we sample 1 million model realizations of  $N_d$  and CCN (e.g., model variants) with 1 million different combinations of parameter values sampled uniformly across 45 dimensional parameter space.

Model variants are ruled out when they are observationally implausible based on a implausibility measure

205

210

215

220

225

230

$$I(x) = \frac{|M - O|}{|Error(M)| + |Error(O)|} > 1 \tag{4}$$

where M is the emulator campaign-mean and O is the observed campaign-mean (Regayre et al., 2020). Error(M) and Error(O) denote the deviation from the emulator campaign-mean and observation campaign-mean, respectively. Error(M) comes from emulator uncertainty and the variance Var(M) in the emulator estimate is directly calculated from GP regression. Error(M) is estimated as  $\pm 1.96*\sqrt{Var(M)}$ . The number of 1.96 is chosen as  $\pm 1.96*\sqrt{Var(M)}$  covers approximately 95% confidence bounds of the emulator uncertainty. Estimating observational uncertainty Error(O) as fractional value is commonly used in observational constraints on models (Johnson et al., 2020; Song et al., 2024). We discuss observational uncertainty in terms of a fractional error  $f_{obs}$ . Finally, we write the implausibility metric I(x) where we account for 95% uncertainty in the emulator and an arbitrary observational uncertainty as

$$I(x) = \frac{|M - O|}{|\sqrt{Var(M)} \cdot 1.96| + |O \cdot f_{obs}|} > 1$$
(5)

Model variants are excluded when I(x) exceeds 1. An illustration of our constraint process is summarized in Figure S3.

In this paper, we vary the observational uncertainty by varying  $f_{obs}$  under two conditions: (1) with emulator uncertainty and (2) without emulator uncertainty, to characterize the impact of different sources of uncertainty on our ability to constrain the response of  $N_d$  to anthropogenic aerosol. We discuss the impact of different values of  $f_{obs}$  on the model constraint process in section 3.4. Eq 5 is a simplified implausibility metric as in Williamson et al. (2013); Johnson et al. (2020). Here, we only consider observational uncertainty and emulator uncertainty in the comparison between 1 million model variants with observations. Spatial-temporal representation uncertainty and model structural uncertainty are also important as discussed in Johnson et al. (2020). We set the spatial-temporal representation uncertainty to 0 in Eq 5 as we collocated the model outputs to flight track locations in 2-min  $\times$  50-meter composites. The characterization of model structural uncertainty is conceptually ambiguous to quantify (Regayre et al., 2023) and is not considered in this work.

#### 2.5 Constraint metric

235

245

250

255

260

We conducted sensitivity tests on the observationally plausible 2.5-97.5th percentile range of  $\Delta N_{d,PD-PI}$  to the emulator and observational uncertainties. The observationally plausible 2.5-97.5th percentile range of  $\Delta N_{d,PD-PI}$  was calculated with varying presumed observation uncertainties. To reduce noise from imperfect emulators, we conduct another set of sensitivity tests with emulator uncertainties set to 0 (Error(M)=0) in Eq 4 in the sensitivity test. The 'constraint' is quantified as the reduction in the observational plausible range relative to the prior range predicted from the 1 million model variants. The relative reduction in range is calculated using

constraint = 1 - 
$$\frac{\text{Posterior: } \Delta N_{d,(PD-PI),\text{obs, }97.5} - \Delta N_{d,(PD-PI),\text{obs, }2.5}}{\text{Prior: } \Delta N_{d,(PD-PI),97.5} - \Delta N_{d,(PD-PI),2.5}}$$
 (6)

Where the subscript 'obs' denotes the sources of observations that are used for constraints. The posterior range refers to the range of observationally plausible  $\Delta N_{d,PD-PI}$  at 2.5-97.5th percentiles. The prior range refers the 2.5-97.5th percentile range of  $\Delta N_{d,PD-PI}$  derived from the original 1-million-member sample. Mathematically, the range of constraint in Eq 6 should vary between 0 to 1. The greater the magnitude, the better constraints we can achieve.

# 2.6 Spaceborne observation

In addition to the comparison between aircraft measurements and model outputs saved along flight tracks, we examine the simulated global oceanic mean  $N_d$  and confront it with observations. Observations of global oceanic  $N_d$  are derived from the Moderate Resolution Imaging Spectroradiometer (MODIS). MODIS is a passive radiometer onboard NASA's Terra and Aqua satellites.  $N_d$  is calculated from MODIS retrievals of effective radius ( $r_e$ ) and optical depth ( $\tau$ ) assuming an adiabatic cloud (Grosvenor and Wood, 2014). MODIS  $N_d$  is calculated for daily means for the period 2003–2015 and is gridded to 1 by 1 degree resolution as in Grosvenor and Wood (2014). During winter, high-latitude regions (e.g., Arctic, Antarctic) have lower greater solar zenith angle (SZA), resulting in lower reflected solar radiation, making retrievals of cloud properties (e.g.,  $r_e$  and  $\tau$ ) less reliable. MODIS  $N_d$  is unavailable during wintertime high latitude regions. To ensure consistency in the comparison between MODIS  $N_d$  and the model data,  $N_d$  data from months and latitudes where MODIS retrievals are unavailable are removed from the ESM dataset. In addition to global oceanic mean  $N_d$  from MODIS, we also examine a box region from MODIS with latitude range of 65 S° - 42 S° and longitude range of 132 E° - 165 E°, which covers the SOCRATES campaign. MODIS  $N_d$  is computed in this box region and compared with campaign-mean  $N_d$  from SOCRATES in-situ measurements.

#### 3 Results

As discussed above, previous studies have evaluated CAM6 in terms of its representation of SO aerosol, cloud, and precipitation characteristics using in-situ observations from SOCRATES (McCoy et al., 2021; Zhou et al., 2021; Gettelman et al., 2020; McCluskey et al., 2023). They found that simulated  $N_d$  is typically too low in CAM6, which is similar to other ESMs (McCoy et al., 2020). However, finding why the SO  $N_d$  is low is complex since  $N_d$  is the result of sources and sinks (Wood et al.,

2012; McCoy et al., 2020; Kang et al., 2022). To understand what leads to biases in  $N_d$  we need to simultaneously consider the impact of multiple processes to tackle the equifinality problem. Briefly, equifinality means multiple combinations of physical processes can result in the same observable state (i.e.  $N_d$ ).

A common suggestion by previous studies is that investigation of aerosol, cloud, precipitation, glaciation, turbulence and activation processes is needed to understand the source of the model  $N_d$  bias (McCoy et al., 2021; Zhou et al., 2021; McCluskey et al., 2023). Here, we examine how different parameter combinations of these processes impact SOCRATES aerosol, clouds, and ACI in CAM6 in section 3.1. By observationally confronting simulations with different parameter combinations, we can evaluate the constrained parameter spaces (Section 3.2) and the likely range of observationally-plausible parameter spaces and their associated range of  $\Delta N_{d,PD-PI}$  (Section 3.3).

# 270 3.1 CCN, $N_d$ and aerosol activation over SOCRATES in CAM6 PPE

265

275

280

285

290

We examine relationships between CCN and  $N_d$  across flight composites (50-meter  $\times$  2-min bin median) within individual PPE members. The number of flight composites valid for CCN- $N_d$  comparisons from SOCRATES in-situ observations is 44 (Figure 2: red dots). This number is smaller than the results in McCoy et al. (2021) as we choose a lower altitude level for analysis with a focus on warm liquid cloud. The number of colocated flight composites valid for CCN- $N_d$  comparisons for each PPE ensemble member (Figure 2: black dots) is less than that from observations (red dots) since some flight composites simulates near-zero  $N_d$  and are excluded from our analysis. This might be due to the coarse vertical resolution of CAM6 and linear interpolation cannot fully capture the  $N_d$  variability in the vertical. Despite the limitations, PPE ensemble members simulate CCN and  $N_d$  flight composites that are comparable with observations.

CCN at 0.2% supersaturation correlates positively with  $N_d$  when comparing matched flight composites along individual flight tracks in the PPE (Figure 2). This is not surprising as we expect CCN at 0.2% supersaturation to be a reasonable proxy for the aerosol particles that activate to form cloud droplets under typical marine boundary layer updraft conditions, consistent with observations (McCoy et al., 2021). Hereafter, we refer to the simulated CCN at 0.2% supersaturation from CAM6 simply as CCN for simplicity. Observations of CCN refer to the observed aerosol concentration with diameters ranging from 0.1  $\mu$ m to 1  $\mu$ m from UHSAS100.

Figure 2 shows a subsample of ensemble members with varying levels of agreement with observations, but a positive correlation between CCN and  $N_d$  in log space is found for most of the PPE members (i.e., 224 out of 262). However, the linear regression slope of  $N_d$  on CCN is high relative to observations for the majority of PPE members (Figure S4a). Because  $N_d$  is a product of both CCN activating into droplets and precipitation removing drops (Wood et al., 2012), a higher CCN- $N_d$  slope in CAM6 does not necessarily indicate a higher simulated aerosol activation efficiency. This diagnostic is broadly telling us that more CCN is required in CAM6 PPE to produce the same amount of  $N_d$  through aerosol activation in the presence of coalescence scavenging compared to observations, particularly at low  $N_d$  concentration (e.g., Figure 2a). Lower  $N_d$  over SOCRATES is associated with increased precipitation rate and greater contribution of coalescence scavenging in controlling  $N_d$  (Kang et al., 2022). The negative correlation between  $N_d$  and precipitation rate is also found in the CAM6 PPE (Figure S5). The high bias in the regression slope of  $N_d$  on CCN in CAM6 PPE may indicate a stronger loss in  $N_d$  from overestimated

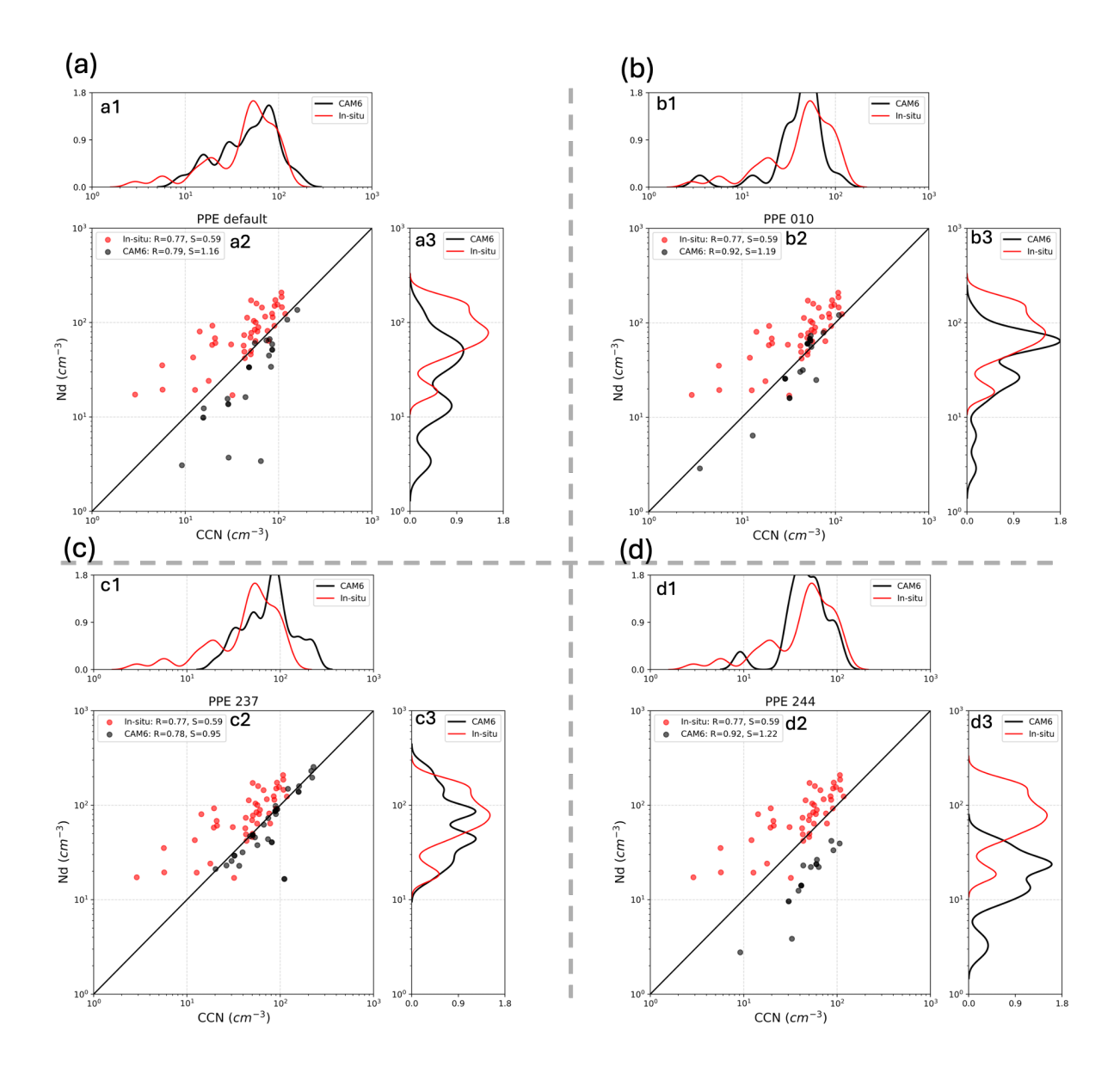


Figure 2. Relationships between SOCRATES CCN and in-cloud cloud droplet number concentration  $(N_d)$  from in-situ measurements (red) and CAM6 members (black), based on flight composites along individual flight tracks (scatters). Flight composites are constructed by binning observations into 50 m (altitude) by 2 min (time) bins for each flight. CAM6 PPE CCN and in-cloud  $N_d$  are collocated to observation composites (50 m × 2 min bins) by linear interpolation for individual PPE members. Bin medians are taken for comparison with CAM6 models following McCoy et al. (2021). CAM6 in-cloud  $N_d$  is computed as  $N_d$  divided by liquid cloud fraction (when cloud fraction  $\leq 1\%$ , we set  $N_d = 0$ ). PDFs of number concentrations of CCN (top) and cloud droplets (right) for matched binned values occurring for CAM6 (black) and observations (red) are shown. (a) Default CAM6 configuration (i.e., PPE simulation for ensemble member 000), (b) PPE simulation for ensemble member 010, (c) PPE 237, (d) PPE 244. PPE members numbered 010, 237 and 244 are chosen to represent cases with varying levels of agreement between the simulated and observed CCN and  $N_d$ .

coalescence scavenging at low  $N_d$  concentration in models. Additionally, the low-biased  $N_d$  may also be influenced by an underestimation of subgrid-scale vertical velocity, turbulence intensity, and other dynamical factors that suppress supersaturation and droplet activation. We verify our hypothesis in the discussion of parameter constraints of CAM6 PPE using observations in section 3.2.

Most of the PPE members simulate  $N_d$  that is low relative to observations, regardless of whether CCN is underestimated (Figure S4, Figure 2). One example is the PPE ensemble of 244 of CAM6 where even though the simulated CCN is relatively close to observations, the  $N_d$  is still biased low. (Figure 2d). This supports the hypothesis in McCoy et al. (2021) that aerosol biases are not the sole contributors to the low  $N_d$  in CAM6, highlighting the importance of other contributing factors.

Although most PPE members exhibit low  $N_d$ , there are some members that are close to observations (Figure S4, Figure 2c). We next compare the PPE with observations to rule out PPE members that are far away from observations (e.g., Figure 2d) and characterize which parameterized processes are important to ACI over SO.

# 3.2 CAM6 parameter constraints from SOCRATES measurements

305

310

315

320

We compare campaign-means of CCN and  $N_d$  because averages reduce random errors of aircraft measurements due to instrument noise, atmospheric turbulence, or other transient variations (Schutgens et al., 2020). Unlike random errors, systematic errors such as sensor miscalibration and systematic sampling cannot be reduced by averaging. The model-observation comparison process follows Eq 5 as detailed in Section 2.4.

Observations of CCN and  $N_d$  identify and constrain physical processes that are important for ACI (Figure 3). We show the 10 most constrained parameters out of 45 in Figure 3. The full list of constrained parameter spaces is shown in Figure S6. By examining how different parameter values are constrained relative to observables we can try to build an understanding of how different processes drive observables. This also illustrates the problem of equifinality where observed values can be arrived at by combining processes in different ways.

Confronting the PPE with observations of CCN constrains aerosol processes (e.g. sea salt emission) and precipitation processes (e.g. autoconversion, accretion) (Figure 3a; the detailed parameter explanation is in Table S1). The sea salt emission scale factor is constrained to higher values, indicating observations of CCN during SOCRATES are consistent with stronger aerosol production in the CAM6 PPE. This is consistent with a lack of aerosol production in CAM6 (McCoy et al., 2021; Zhou et al., 2021).

Constraints on precipitation processes point to the importance of precipitation as an aerosol sink. One of the key parameterization in warm cloud in climate models is the autoconversion, which represents the rate of initial rain formation through collision-coalescence between small cloud droplets.

We can make sense of the relationship between CCN and the autoconversion parameters by looking at how the rate of rain creation through autoconversion works in CAM6. Autoconversion in CAM6 is written as (Khairoutdinov and Kogan, 2000; Gettelman et al., 2015):

$$\left(\frac{\partial q_c}{\partial t}\right)_{\text{auto}} = a \cdot q_c^b \cdot N_d^{-c} \tag{7}$$

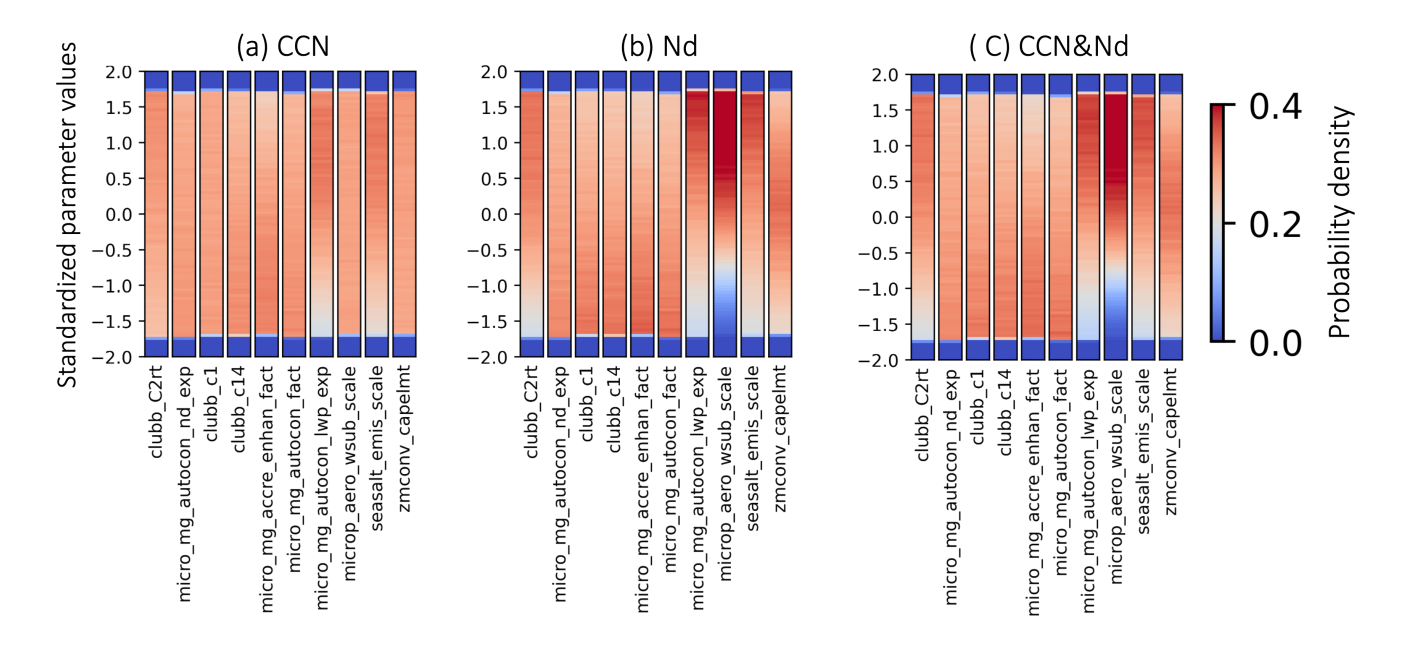


Figure 3. 10 parameters with constrained parameter spaces with observations of (a) CCN, (b)  $N_d$  and (c) CCN &  $N_d$ . Parameter spaces are standardized with mean 0 and variance 1. Warmer colors mean a higher intensity and more data points in that range.

where  $\left(\frac{\partial q_c}{\partial t}\right)_{\rm auto}$  is the rate of generation of rain from cloud water. The autoconversion rate depends on the cloud droplet concentration ( $N_d$  [cm<sup>-3</sup>] in Eq 7) and cloud water content ( $q_c$  [kg/kg] in Eq 7). a, b and -c are uncertain parameters perturbed in the CAM6 PPE (Table S1). They are micro\_mg\_autocon\_fact, micro\_mg\_autocon\_lwp\_exp and micro\_mg\_autocon\_nd\_exp, respectively. Selecting parts of parameter space that are consistent with observations of CCN leads to lower autoconversion scale factors (a in Eq 7) (less efficient rain production by cloud). The effect of larger exponents on liquid water content (b in Eq 7) on the rain production depends on the relative magnitude of liquid water content  $q_c$ . Larger b can result in thicker clouds that precipitate more efficiently under conditions of  $q_c > 1$  kg/kg. A reversed effect can happen under conditions of  $q_c < 1$  kg/kg. The condition of  $q_c > 1$  kg/kg seems unlikely during SOCRATES campaign observations and model simulations (Khairoutdinov and Kogan, 2000; Gettelman et al., 2020). Overall, this results in a lower rain rate across cloud liquid water content values when the scale factor is minimized and the exponent is maximized for the liquid water content in typical stratocumulus clouds (Figure S7). The shift to lower rain rate with observational constraints in CAM6 PPE indicates that rain rate and the loss of CCN from precipitation scavenging are overestimated for the majority of members in CAM6 PPE.

330

335

Observations of  $N_d$  from SOCRATES constrain parameters related to aerosol and precipitation process (Figure 3b), consistent with the findings in Wood et al. (2012) and Kang et al. (2022); McCoy et al. (2020) that the  $N_d$  budget is a function of a source of droplets from CCN and sink from collision-coalescence. The constraint on initial rain formation rate during autoconversion (Eq 7) and the constraint on the strength of precipitation suppression are consistent with CCN observations (Figure 3ab). Broadly, constraints on precipitation formation are consistent with a weaker sink of cloud droplets as well as less cloud

droplet removal via precipitation. This supports the hypothesis in Section 3.1 that rain rate and the loss of  $N_d$  from precipitation scavenging are overestimated for the majority of members in CAM6 PPE. We also want to note that the SO is dominated by supercooled liquid cloud (Gettelman et al., 2020; McCluskey et al., 2023), making the glaciation (Bergeron–Findeisen Process: water vapor deposits onto ice crystals) important in this region. This means that the growth of ice crystals might be an important sink for  $N_d$ . However, we believe the  $N_d$  loss from freezing is minimal when our analysis is restricted to the altitudes below 2 km. This is because a large fraction of snow melts and contributes to rain precipitation at low altitudes (Figure 2 in Field and Heymsfield (2015)). Mixed-phase and ice cloud processes are important in initiating rain as most rain is derived from ice that has melted to form rain (Bergeron, 1935). However, the importance of ice processes is not apparent in our process constraint focused on warmer clouds (Figure S6). McCluskey et al. (2023) examined ice processes over SOCRATES using observations of detailed aerosol and ice nucleating particle (INP) measurements and models (e.g., CAM6), but the process constraints on ice processes with observations of INPs is beyond the scope of this study.

The parameter constraints from observations of  $N_d$  are more stringent than the constraints resulting from using observations of CCN. This is consistent with  $N_d$  being the emergent product of aerosol and precipitation processes (Wood, 2012). In addition to aerosol and precipitation processes, mechanisms important for aerosol activation are also constrained by  $N_d$  observations (Figure 3b), such as deep convection (e.g., zmconv\_capelmt), subgrid velocity (e.g., microp\_aero\_wsub\_scale), and turbulence (e.g., CLUBB: Cloud Layers Unified by Binormals parameters in table S1), as they play a role in vertical aerosol transport and in generating supersaturation. In particular, microp\_aero\_wsub\_scale is efficiently constrained to higher values, suggesting an underestimated subgrid velocity (i.e., lower updraft speed) that suppresses supersaturation, leading to lower  $N_d$ .

Finally, we examine the effect of constraining the PPE using observations of both  $N_d$  and CCN. The effect of combining these constraints is similar to the constraint arrived by  $N_d$  alone (Figure 3c). This is consistent with  $N_d$  being an emergent property of both aerosol processes and cloud and precipitation processes.

Observations of CCN and  $N_d$  during SOCRATES constrain aerosol, precipitation, and cloud processes. In the next section we examine whether the process constraint from observations of CCN and  $N_d$  constrains the response of  $N_d$  due to anthropogenic aerosol. Precipitation rate would be a useful constraint on the response of  $N_d$  as both observations of CCN and  $N_d$  constrain precipitation process as discussed in this section. However, the path to including an observational constraint of cloud base precipitation is somewhat opaque and is not included here. Light precipitation rate at cloud base can be retrieved using radar-lidar techniques (Kang et al., 2022), but to provide an apples-to-apples comparison to CAM6 in terms of cloud base precipitation we believe that an instrument simulator is needed (Silber et al., 2022).

# 3.3 Observationally plausible $\Delta N_{d,PD-PI}$ from SOCRATES measurements

345

350

355

360

365

370

As discussed in the previous section, observations of  $N_d$  and CCN constrain the range of possible process representations. In turn, these same processes drive the response of  $N_d$  to anthropogenic aerosol. This results in a strong correlation between PD  $N_d$  and PI  $N_d$  (Figure 4; black line) and by extension the change in  $N_d$  between PI and PD (Figure 4; orange line) in the CAM6 PPE. The fractional change in  $N_d$  ( $\Delta lnN_d$ ) is computed by taking the slope of  $\Delta N_{d,PD-PI}$  to  $N_d$  following the definition from Bellouin et al. (2020). The  $\Delta lnN_d$  predicted by the CAM6 PPE (0.23) is greater than the expert elicitation

range from Bellouin et al. (2020) (i.e., 0.05 to 0.17) (Figure 4). The emergent relationship between PD  $N_d$  (observable) and the  $\Delta N_{d,PD-PI}$  (unobservable) with a r-value of 0.95 can be used to constrain the likely range of  $\Delta N_{d,PD-PI}$  if we know the possible range of PD  $N_d$  (observable). As suggested in Klein and Hall (2015), emergent relationships used for constraints require process-level understanding. We explain the emergent behavior from CAM6 PPE (Figure 4) using a sink-source model of  $N_d$  in Section 3.3.2

380

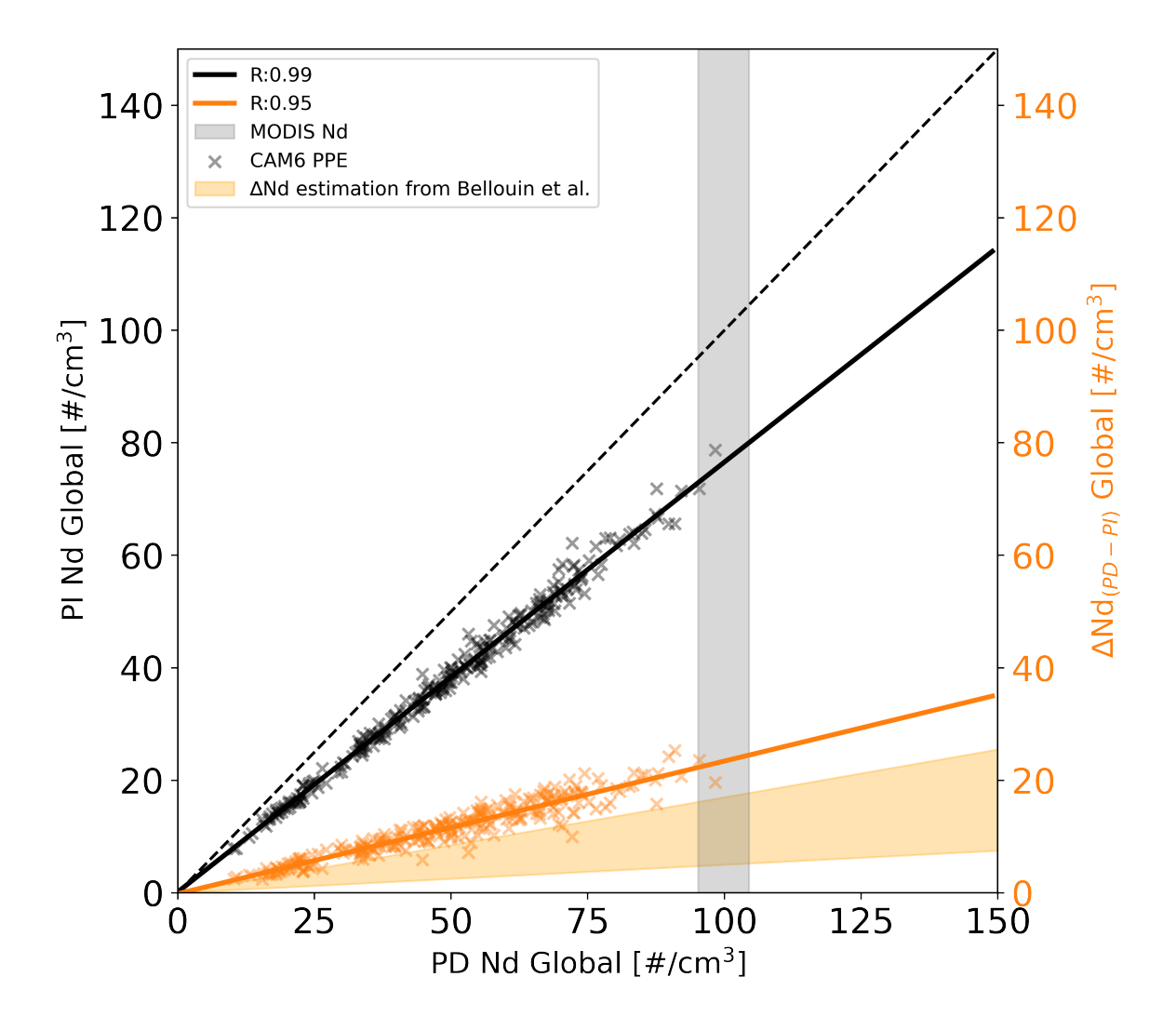


Figure 4. Global oceanic mean of preindustrial (PI)  $N_d$  (black) and  $\Delta N_{d,PD-PI}$  (orange) as a function of present-day (PD) oceanic  $N_d$  from CAM6 PPE members (x-shaped markers). The 95% confidence on the interannual range of global oceanic mean  $N_d$  from MODIS is shown in the gray vertical bar. The estimated  $\Delta N_{d,PD-PI}$  based on the fractional change in  $N_d$  ( $\Delta lnN_d$ ) from Bellouin et al. (2020) is shown in the orange shading.

### 3.3.1 Constraint using regional measurements

385

390

395

405

410

One question is whether SOCRATES, a field campaign over the SO where natural aerosols dominate, can be used to constrain the perturbation in  $N_d$  globally. SOCRATES samples natural aerosols and microphysical processes in a pristine environment (McCoy et al., 2021; McFarquhar et al., 2021), but it is not entirely isolated from the effects of anthropogenic aerosol emissions (Figure 1a). This is consistent with Hamilton et al. (2014), who show that the SO in the present day atmosphere is not always pristine. In addition to aerosol availability acting as a source for the  $N_d$  budget, both  $N_d$  and natural or anthropogenic aerosols share similar removal pathways through precipitation scavenging (Zheng et al., 2024; Wood et al., 2012; Kang et al., 2022), making the processes sampled during SOCRATES relevant for understanding the  $N_d$  perturbations on a global scale.

Another question is simply how representative is the  $N_d$  observed in the sample from SOCRATES of the global mean. Across the PPE, the campaign-mean  $N_d$  over SOCRATES correlates with the global, oceanic-mean of  $N_d$  with an explained variance of 0.36 across the PPE members (Figure 5). This positive correlation in  $N_d$  is reasonable as processes that govern droplet activation and removal of  $N_d$  share similarities over the global ocean and in the SO. The removal of  $N_d$  is primarily due to the precipitation scavenging (Wood et al., 2012; Kang et al., 2022). The relationship between the amount of CCN and the resultant  $N_d$  contain information about this sink term as well as the transport of CCN to cloud.

The relationship between SOCRATES  $N_d$  and the global mean also speaks to the importance of the marine, pristine baseline of aerosol in setting  $N_d$ . Previous studies underline the contribution of the oxidation of DMS (McCoy et al., 2015), sea spray (Wood et al., 2012; McCoy et al., 2015; Kang et al., 2022), and transportation of anthropogenic aerosols from continents (Wood et al., 2012; McCoy et al., 2018) to oceanic CCN.

Observational records also show consistency in the amount of  $N_d$  between the SO and the globe. Spaceborne observations of SOCRATES campaign-mean  $N_d$  and global-mean  $N_d$  are relatively consistent (Figure 5: black dot). In-situ campaign-mean  $N_d$  (Figure 5: gray dashed line) is slightly less than spaceborne observations (Figure 5: black dot), while the difference is small despite originating from entirely different methodologies.

We hasten to point out that we are not trying to argue that SOCRATES is sufficient to provide a complete picture of global-scale processes. However, SOCRATES does illustrate the utility of investigating even a single field campaign in this framework. Including additional campaigns in future field is likely to provide additional constraint on global-scale processes.

# 3.3.2 Constraint from present day observations

 $N_d$  sampled during SOCRATES contains information for globally-relevant processes (Figure 5), but do PD observations of aerosol and cloud properties constrain the anthropogenic perturbation in  $N_d$ ? We find this to be the case in the context of the PPE. To dissect the causes of the relationship between PD  $N_d$  and PI  $N_d$ , the relationship between PD  $N_d$  and  $\Delta N_{d,PD-PI}$  and the relationship between CCN and  $N_d$  we turn to a simple budget model of  $N_d$ . Based on Wood et al. (2012); Kang et al. (2022), the  $N_d$  budget model is described as a function of source of CCN and sink from precipitation scavenging

$$N_{d,PD} = \frac{\left[CCN_{\text{FT}} + \frac{F(\sigma)U_{10}^{2.8}}{Dz_i}\right]}{\left[1 + \frac{hKP_{\text{CB}}}{Dz_i}\right]}$$
(8)

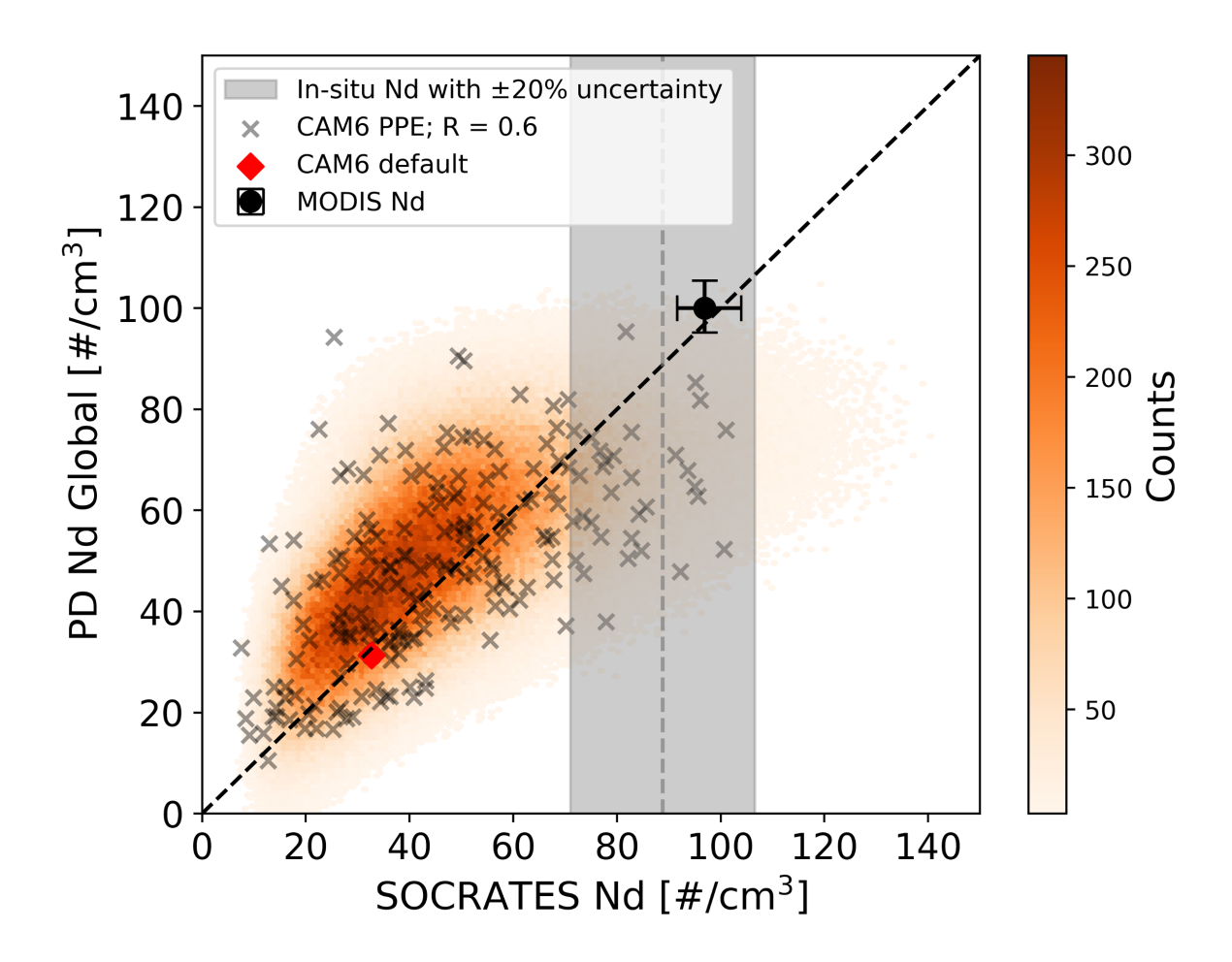


Figure 5. Global oceanic mean of present day (PD)  $N_d$  versus SOCRATES campaign-mean  $N_d$  from the CAM6 PPE members (x-shaped markers), 1M emulations from the PPE (orange color shading indicates density) and observations. The black dot shows the observational global-mean  $N_d$  and campaign-mean  $N_d$  calculated from MODIS, with its 95% confidence interval based on the interannual range. Observational SOCRATES campaign-mean  $N_d$  from SOCRATES in-situ measurements is shown as the vertical dashed line with an uncertainty of  $\pm 20\%$  from the campaign-mean.

In Eq 8, the parameterized source of CCN is from free troposphere  $CCN_{FT}$  and surface contribution  $\frac{F(\sigma)U_{10}^{2.8}}{Dz_i}$  (e.g., sea spay aerosol), where  $F(\sigma)$  is the sea spray function that depends on supersaturation (Clarke et al., 2006) and  $DZ_i$  is the subsidence rate at cloud top, which is used an approximate for entrainment rate (McCoy et al., 2020). For the precipitation sink term  $\frac{hKP_{\text{CB}}}{Dz_i}$ , h is the cloud thickness, K is a constant that depends on the collection efficiency of cloud droplets and  $P_{CB}$  is the rain rate at cloud base (Wood, 2006). The  $N_d$  budget model has been used to predict the  $N_d$  amount with confidence over the subtropic and mid-latitudes (Mohrmann et al., 2018; Zheng et al., 2018; Kang et al., 2022).

In this study, we follow the basic source-sink model idea from Wood et al. (2012) but we simplify the  $N_d$  budget model to fewer terms for a conceptual understanding of the relationships between variables. The  $N_d$  budget model is written as

$$N_d = \frac{\lambda \cdot CCN}{1 + k_{remo} \cdot P_{CR}} \tag{9}$$

Instead of parameterizing CCN source from free troposphere  $CCN_{FT}$  and surface contribution  $\frac{F(\sigma)U_{10}^{2.8}}{D_{z_i}}$ , we characterize CCN source as  $\lambda \cdot CCN$ , where  $\lambda$  is a scale factor that accounts for the amount of CCN that can be activated to cloud droplets depending on the vertical updraft, relative humidity, size and hygroscopicity of CCN, etc.  $\lambda$  varies from 0 to 1. For precipitation sink term  $\frac{hKP_{CB}}{Dz_i}$ , we simplified it as  $k_{remo} \cdot P_{CB}$ , where  $k_{remo}$  equals to  $\frac{hK}{Dz_i}$ . It accounts for the rate of loss of  $N_d$  from precipitation. To estimate  $k_{remo}$ , we set  $K = 2.25 \text{ m}^2 \text{ kg}^{-1}$ , subsidence rate  $Dz_i = 4 \text{ mm s}^{-1}$  following Wood et al. (2012); Kang et al. (2022); McCoy et al. (2020). Cloud thickness h is set to 300 m, which is a typical magnitude for marine clouds (Wood, 2012). Changing cloud thickness h to smaller (e.g., 100 m) or larger values (e.g., 500 m) does not significantly change our results.

In this idealized set up, the CCN source  $(\lambda \cdot CCN)$  and precipitation sink  $(k_{remo} \cdot P)$  are set to be the same between PI and PD. This is a reasonable assumption for CAM6 PPE as its parameter setup is the same in the paired PI and PD simulations. The only difference between PI and PD is the amount of CCN. Therefore, we can write  $N_d$  budget model in PI and PD as

$$N_{d,PI} = \frac{\lambda \cdot CCN}{1 + k_{remo} \cdot P_{CB}} \tag{10}$$

$$N_{d,PD} = \frac{\lambda \cdot (CCN + \Delta CCN)}{1 + k_{remo} \cdot P_{CB}} \tag{11}$$

where  $\Delta CCN$  in Eq 11 stands for CCN from anthropogenic aerosol emissions. Eq 10 and Eq 11 allow for a simplified representation of the underlying physical processes driving  $N_d$  budget in PI and PD.  $\Delta N_{d,PD-PI}$  can be calculated by taking the difference between Eq 11 and Eq 10

435

$$\Delta N_{d,PD-PI} = \frac{\lambda \cdot \Delta CCN}{1 + k_{remo} \cdot P_{CB}} \tag{12}$$

We evaluate the relationship between  $\Delta N_{d,PD-PI}$  and PD  $N_d$ , CCN and  $N_d$  using the budget models. We calculate the  $\Delta N_{d,PD-PI}$  and PD  $N_d$  in response to a anthropogenic perturbation of  $+\Delta CCN$  at varying precipitation rate  $P_{CB}$  and CCN scale factor  $\lambda$ . With this simplified set up,  $\Delta N_{d,PD-PI}$  and PD $N_d$ , CCN and  $N_d$  are positively correlated (Figure 6), consistent with the CAM6 PPE (Figure 2, Figure 4). At larger precipitation rate P, more CCN is needed to activate to form the

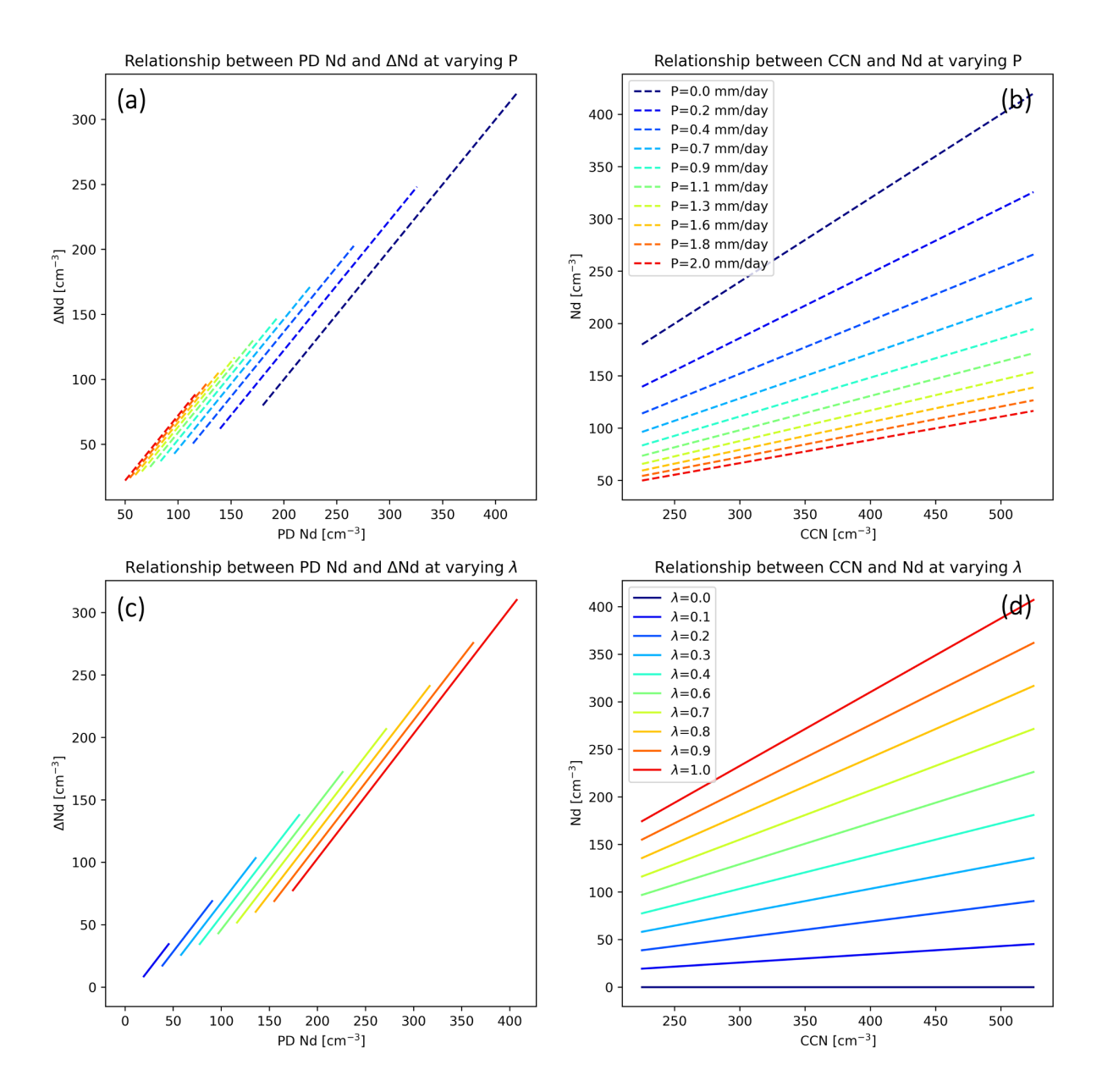


Figure 6. Idealized relationships based on the source-sink model of the  $N_d$  budget (Eq 8 in Wood et al. (2012) with modifications). (a)  $\Delta N_{d,PD-PI}$  versus PD  $N_d$  based on Eq 11 and Eq 12 at varying precipitation rate P. P is set to vary from 0 to 2 mm/day in 10 equal increments. The varying P is within the observational range in Wood et al. (2012). CCN is set to 125 cm<sup>-3</sup> as a background CCN from natural source.  $\Delta$ CCN is set to be varying between 100 to 400 cm<sup>-3</sup> with 20 equal increments.  $k_{remo}$  is set to 0.8. (b)  $N_d$  versus CCN at varying precipitation rate P with the same model setup as (a). (c)  $\Delta N_{d,PD-PI}$  versus PD  $N_d$  at varying CCN scale factor  $\lambda$ . Precipitation rate P is set to 0.2 mm/day. (d)  $N_d$  versus CCN at varying  $\lambda$  with the same model setup as (c).

same amount of  $N_d$  (Figure 6b). This leads to an overall lower  $N_d$  and  $N_d$  change due to aerosols at high precipitation rate (Figure 6a). With more CCN amount (or larger  $\lambda$ ), there is a higher  $N_d$  and  $N_d$  change due to aerosols (Figure 6cd). These results suggest that the positive correlations in CAM6 PPE members are driven by sink from precipitation scavenging and source from CCN as depicted in the idealized model.

Understanding the positive relationships in CAM6 PPE we can use PD observations of  $N_d$  to constrain unobservable quantities such as perturbations in  $N_d$  due to anthropogenic aerosols. To constrain global-mean quantities, we use observations of  $N_d$  from SOCRATES campaign as the variance in global oceanic-mean  $N_d$  is largely explained by SOCRATES campaignmean  $N_d$  (Figure 5). In addition to PD  $N_d$  observations, we use the observed aerosol concentration from UHSAS100 from SOCRATES as a proxy of CCN to provide an additional constraints on  $\Delta N_{d,PD-PI}$  as the parameter spaces of the PPE have been shown to be constrained by CCN in Section 3.2 (Figure 3a). Precipitation processes are constrained by both observations of CCN and  $N_d$  as discussed in secton 3.2. Inspired by this, we wanted to examine the effects of cloud base precipitation on the constraints on  $\Delta N_{d,PD-PI}$ . However, we found it difficult to make a direct comparison between CAM6 and cloud radar–lidar–retrieved precipitation rates at cloud base. Therefore, our constraints on  $\Delta N_{d,PD-PI}$  focus on observations of CCN and  $N_d$ . Nonetheless, we provide an illustration of what the constraints would behave if observed precipitation rates were used, based on idealized sensitivity tests discussed in Section 3.3.3.

# 3.3.3 Constraints from CCN and $N_d$ measurements

445

455

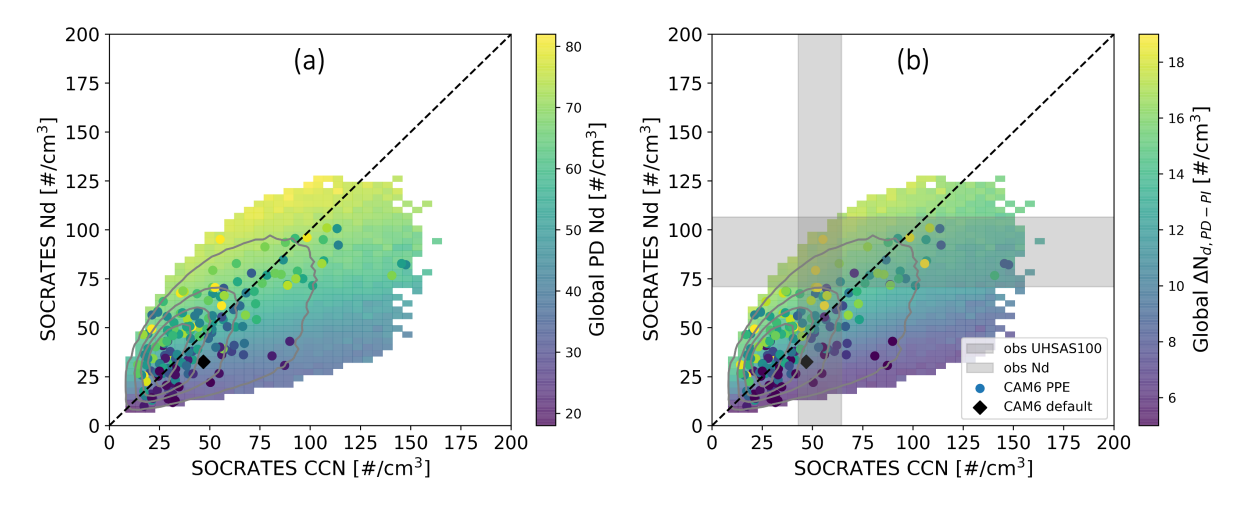


Figure 7. (a) SOCRATES campaign-mean  $N_d$  versus campaign-mean CCN and colored by present-day  $N_d$  from the CAM6 PPE members (color dots) and 1M emulations from the PPE (color shading). Emulate density is shown in solid contours. (b) The same with (a) but colored by  $\Delta N_{d,PD-PI}$ . The color shading shows 2D bin-averaged values of (a) global mean  $N_d$  and (b)  $\Delta N_{d,PD-PI}$ , computed using  $60\times60$  bins in SOCRATES CCN and SOCRATES Nd space. This smoothing highlights large-scale patterns while excluding sparsely sampled regions. Colored points show individual PPE members without averaging. Observational SOCRATES campaign-mean CCN (i.e., UHSAS100) and  $N_d$  from SOCRATES in-situ measurements is shown as the gray shaded bars with an uncertainty of  $\pm20\%$  from the campaign-mean.

Before going into the constraints, we first examine the aerosol activation across the PPE members with different parameterizations. Campaign-mean CCN and  $N_d$  are positively correlated across PPE ensembles (Figure 7a), consistent with the CCN- $N_d$  relationship across flight composite in individual models (Figure 2) and the idealized model (Figure 6ac).

460

Understanding emergent relationships is essential in constraining unobservable quantities (Klein and Hall, 2015). With the idealized  $N_d$  budget model (Figure 6), we have understood how the physical processes (i.e., source of  $N_d$  from CCN; sink of  $N_d$  from precipitation scavenging) are related to the correlations between variables across the CAM6 PPE (Figure 2, Figure 4). Next, we use airborne observations of CCN and  $N_d$  to rule out implausible model variants out of the 1 million variants emulated from the CAM6 PPE (Figure 7b) following the implausibility metric (Eq 5). The prior 2.5-97.5th percentile range of  $\Delta N_{d,PD-PI}$  is 3.6 cm<sup>-3</sup> to 19.8 cm<sup>-3</sup>. Based on the implausibility metric (Eq 5), observations of CCN have no effect on the constraints on  $\Delta N_{d,PD-PI}$ . Using the same implausibility metric, observations of  $N_d$  over SOCRATES constrains the range of  $\Delta N_{d,PD-PI}$  to be 6.1 cm<sup>-3</sup> to 20.4 cm<sup>-3</sup> at the 2.5-97.5th percentile, equivalent to 12% reduction in range and the median increases by 16% (Figure 8a). The constraints on  $\Delta N_{d,PD-PI}$  are also consistent with the results in Song et al. (2024) that utilizes hemispheric contrast of  $N_d$  as a proxy to  $\Delta N_{d,PD-PI}$  using observations of remote sensing from MODIS, indicating the consistencies between measurements of  $N_d$  from different observing techniques.

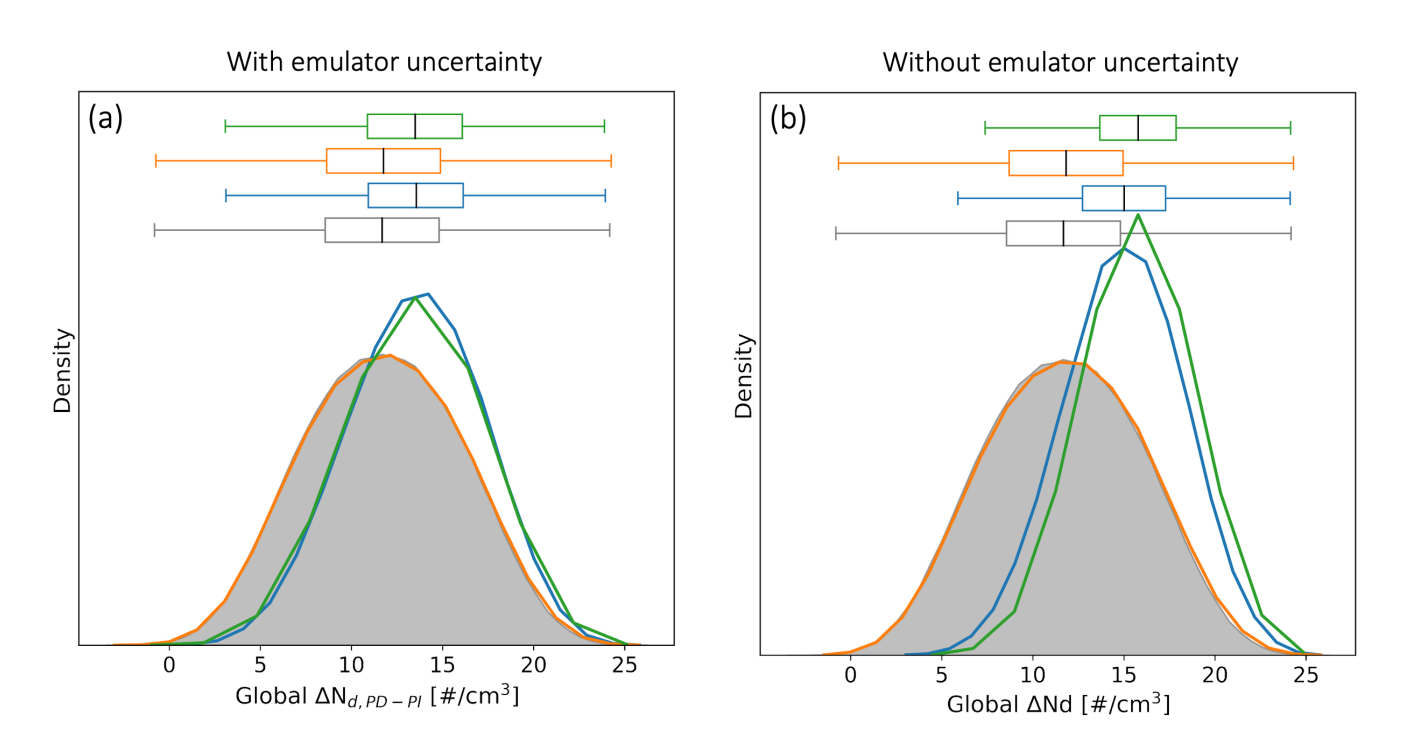


Figure 8. The distribution of emulated  $\Delta N_{d,PD-PI}$  prior (grey shading), and observationally-constrained posterior from SOCRATES observed CCN only (orange),  $N_d$  only (blue), and CCN and  $N_d$  (green). (a) With emulator uncertainty. (b) without emulator uncertainty.

In this study, the emulator predictions are based on emulator mean predictions (i.e., M in Eq 4) and emulator uncertainties (i.e., Error(M) in Eq 4). Although the emulator mean predictions are overall good, the emulator uncertainty created for CAM6 PPE outputs are relatively large (Figure S2). This may have a huge impact on the model-observation comparison process (Figure S3, Eq 4). We therefore examine the constraints on  $\Delta N_{d,PD-PI}$  without the effects of emulator uncertainties (i.e., set Error(M)=0 by setting the number of variance to 0 (i.e.,  $0*\sqrt{Var(M)}$ ) in Eq 5) to check whether this change significantly affects our constraints. The implausibility metric in this case follows

$$I(x) = \frac{|M - O|}{|O * 20\%|} > 1 \tag{13}$$

Consistencies are found in the observational constraints on  $\Delta N_{d,PD-PI}$  under conditions both with and without emulator uncertainties. Observations of CCN have no effect on the constraints under both conditions (Figure 8), suggesting that the zero constraint from CCN is not a result of large emulator uncertainties. Instead, the near zero constraint on  $\Delta N_{d,PD-PI}$  from CCN might be because the CCN provides less information about the number of cloud droplets that can form through aerosol activation compared to direct measurements of cloud droplet numbers. Although CCN number concentration at a given supersaturation accounts for a certain level of chemical composition of aerosols (i.e., hygroscopicity and size), environmental conditions, which is critical for their activation to cloud droplets, is less known. The observational constraints on  $\Delta N_{d,PD-PI}$  from SOCRATES  $N_d$  are consistent in both conditions in terms of the positive shift in the likely range of  $\Delta N_{d,PD-PI}$ . Observations of  $N_d$  narrow the  $\Delta N_{d,PD-PI}$  range more efficiently under the condition without emulator uncertainties than under the condition with emulator uncertainties. The reduction in range of  $\Delta N_{d,PD-PI}$  is 21% and the increase in the median is 28% when calculated without emulator uncertainties (Figure 8b).

480

485

490

495

500

Observations of CCN and  $N_d$  consistently constrain aerosol and precipitation processes as we discussed in section 3.2 so we examined their joint effects on  $\Delta N_{d,PD-PI}$  in Figure 8. We found great improvement on the  $N_d$  constraint when including the effects of CCN, assuming no emulator uncertainty (Figure 8b). The  $\Delta N_{d,PD-PI}$  range is narrowed down by 27% and the median shifts from 11.7  $cm^{-3}$  to 15.5  $cm^{-3}$  (i.e., 35% increase in median). The result suggests that the direction (e.g., positive or negative shift) of the constraint on  $\Delta N_{d,PD-PI}$  is not sensitive to emulator uncertainty, while the strength of constraints is sensitive to emulator uncertainty.

Precipitation scavenging works as a sink for both CCN and  $N_d$  (Figure 6ab), suggesting the strong potential of using precipitation rate as an observational constraints on  $\Delta N_{d,PD-PI}$ . We found it is difficult to make apples-to-apples comparison between CAM6 and cloud radar-lidar retrieved precipitation rate at cloud base. Therefore, we do not use observed precipitation rates in this study. Instead, we examine what the constraints on  $\Delta N_{d,PD-PI}$  would respond under two hypothetical campaignmean surface precipitation rate constraints, used as idealized sensitivity tests. The results suggest that surface precipitation rate has no constraint on  $\Delta N_{d,PD-PI}$  (Figure S8). The zero constraint might be due to surface precipitation rate is less informative than cloud base precipitation rate on the  $N_d$  budget due to the evaporation during descent. Another possible explanation is that while the precipitation sink explains a lot of variance from flight to flight, (Kang et al., 2022), it doesn't vary as dramatically between ensemble member representations of the entirety of the campaign mean because it is strongly controlled by the amount of water vapor and circulation. Overall, we believe further development of instrument simulators for simulating cloud

base precipitation rate for global models is needed to improve our ability to leverage airborne cloud base precipitation rate to constrain global behavior.

As discussed in Section 2.4, using UHSAS100 as a proxy to CCN at 0.2% (CCN02) supersaturation may underestimate the observed CCN02. We conduct a sensitivity test on the constraints on  $\Delta N_{d,PD-PI}$  by increasing  $\Delta N_{d,PD-PI}$  by increasing the observed CCN by 8% to 40%, according to the CCN02based on the 25th to 75th percentile range of the CCN0.2:UHSAS100 ratio uncertainty shown in Figure S2a in of McCoy et al. (2021). The results suggest that increasing the observed CCN does not significantly affect the constraint on  $\Delta N_{d,PD-PI}$  (Figure S9).

# 3.4 Sensitivity tests on the observationally plausible $\Delta N_d$

505

510

520

525

530

535

The uncertainty associated with airborne measurements of aerosol and cloud microphysics is difficult to define as a fixed value because it depends on multiple sources of uncertainties such as: sampling error due to limited spatial and temporal coverage of flight tracks, variability in flight patterns (e.g., altitude, and positioning relative to cloud features), instrument noise due to environmental variability (e..g., turbulence, wind shear). Therefore, assuming a fixed observation uncertainty of  $\pm 20\%$  for airborne measurements in Section 3.3.3 is just a to provide a baseline amount of uncertainty.

In this section, we perform sensitivity tests on the observationally plausible  $\Delta N_{d,PD-PI}$  by the varying observational uncertainty under conditions of with emulator uncertainty (i.e.,  $\text{Error}(M) = \pm 1.96 * \sqrt{Var(M)}$  in Eq 5) and without emulator uncertainty (i.e.,  $\text{Error}(M) = 0 * \sqrt{Var(M)}$  in Eq 5). Systematic uncertainty in the observations is assumed to vary from  $\pm 5\%$  to  $\pm 100\%$  for the campaign-mean. The constraints on  $\Delta N_{d,PD-PI}$  is calculated as the reduction in the 2.5-97.5 percentile range of  $\Delta N_{d,PD-PI}$  following Eq 6.

Figure 9 shows the constraints on  $\Delta N_{d,PD-PI}$  by observations of CCN (orange line),  $N_d$  (blue line) and combining CCN and  $N_d$  (green line). Overall,  $\Delta N_{d,PD-PI}$  is more tightly constrained without emulator uncertainty (Figure 9bd), which makes sense as excluding emulator uncertainties (i.e., Eq 13) allows more model variants to be excluded during model-observation comparison relative to Eq 5. The constraints on  $\Delta N_{d,PD-PI}$  under two conditions (i.e., with and without emulator uncertainty) both have a positive shift in the 2.5-97.5 percentile range (Figure 9cd), suggesting the constraints are not a result of noise from emulator uncertainties.

Consistent with Figure 7, observations of CCN provide nearly no constraint on  $\Delta N_{d,PD-PI}$  regardless of the uncertainty in CCN (Figure 9: orange line). With increasing uncertainties from airborne measurements of  $N_d$ , the plausible range of  $\Delta N_{d,PD-PI}$  is less constrained under both conditions of with and without emulator uncertainty (Figure 9: blue line). The weakened constraints on  $\Delta N_{d,PD-PI}$  with increasing uncertainties in observations is due to the retention of more model variants as plausible during model-observation comparison process (Figure S3), thereby exacerbating the equifinality problem (Johnson et al., 2020), for which increasing number of plausible parameter combinations results in broader parameter spaces and thereby reduced constraints on  $\Delta N_{d,PD-PI}$  (Figure 9ab).

The reduction in ranges (constraints) becomes negligible with observation uncertainty of  $N_d$  reaching  $\pm 75\%$  under the condition with emulator uncertainty (Figure 9a). The threshold of observational uncertainty of  $N_d$  that can achieve constraints is a bit larger under the condition without emulator uncertainty, which is  $\pm 85\%$  (Figure 9b), suggesting skillful emulators play

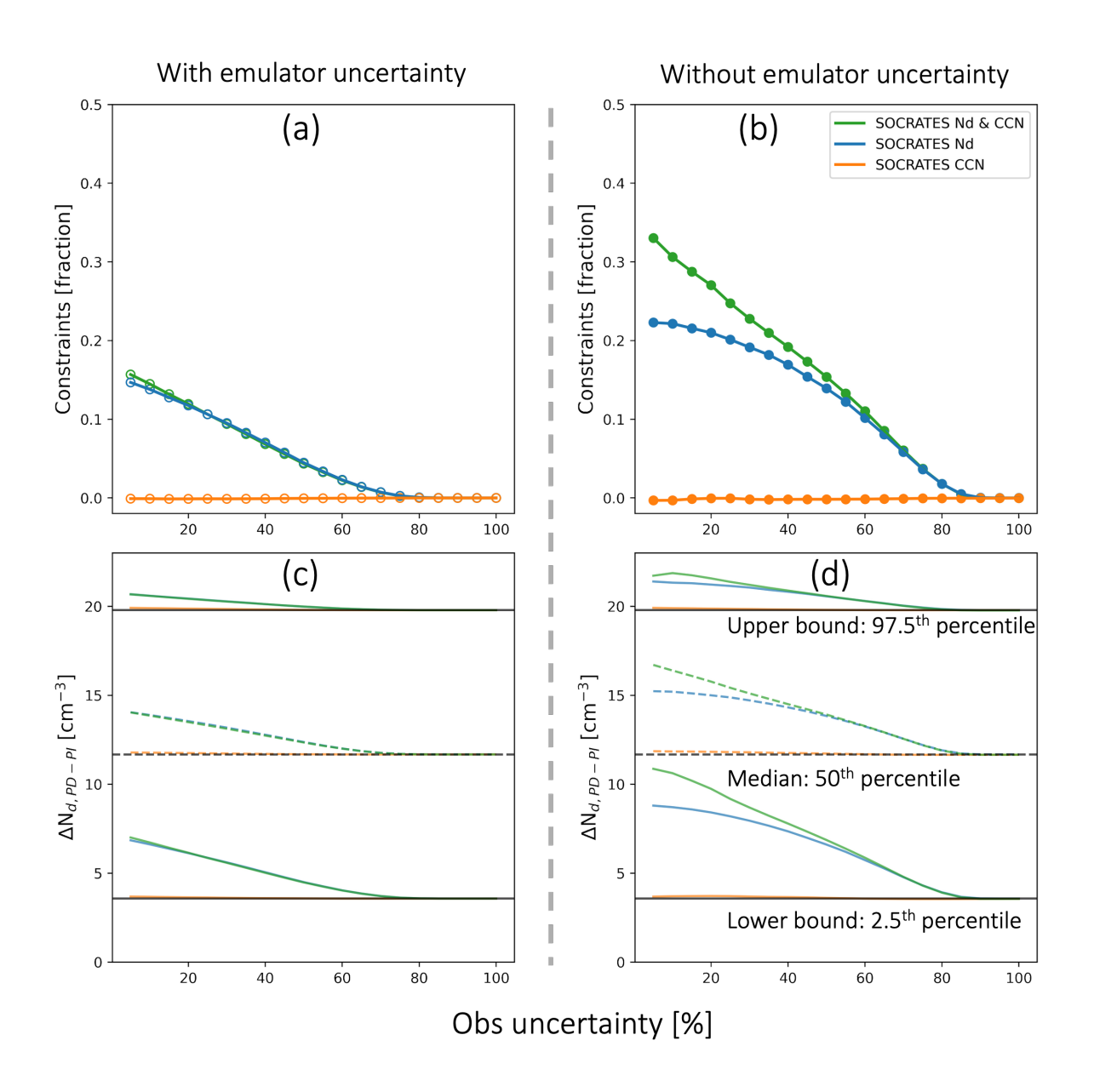


Figure 9. (a) The reduction in the observationally-constrained 2.5-97.5 percentile range of  $\Delta N_{d,PD-PI}$  relative to the emulation prior range with increasing aircraft measurements uncertainties with emulator uncertainties considered, following the implausibility metric as described in Eq 5. Observations are from SOCRATES CCN from UHSAS100 (orange),  $N_d$  from CDP (blue) and both observations (green). Uncertainty ranges from  $\pm 5\%$  to  $\pm 100\%$  from the campaign-mean with 5% equal increments. (b) The same (a) but without emulator uncertainty, following the implausibility metric described as Eq 13. (c) The 2.5th, 50th and 97.5th percentile value of the observationally-constrained  $\Delta N_{d,PD-PI}$  from SOCRATES CCN (orange),  $N_d$  (blue) and both lines of observations (green) as a function of aircraft measurements uncertainties. (d) The same with (c) but without the effects of emulator uncertainty.

an important role in advancing our constraints. Again, we view uncertainty from emulation as an eminently tractable problem compared to developing a better understanding of instrumental systematic uncertainty. Improving emulator uncertainty can be achieved by creating PPEs that can be easily emulated through a more careful selection of perturbed parameters and an increased amount of training data.

Another key insight from Figure 9 is that the improvement in constraint when both  $N_d$  and CCN are considered emerges at low observational uncertainties for both measurements (Figure 9ab: green line is above the blue). The improved constraint is also found in Regayre et al. (2023) that adding the number of constraint variables with no structural inadequacies improve the constraints on aerosol forcing when their constraints are consistent across multiple observation types. In our work, although the constraints on  $\Delta N_{d,PD-PI}$  by observations of CCN is minimal, the constraints on parameter spaces by airborne observations of CCN and  $N_d$  are consistent (Figure 3), resulting in the improved constraints on  $\Delta N_{d,PD-PI}$ . The improvement of the constraints on  $\Delta N_{d,PD-PI}$  only happens with small uncertainties associated with airborne measurements (Figure 9ab: green line), highlights the importance of accurate airborne measurements of aerosol and cloud properties on constraining  $\Delta N_{d,PD-PI}$ .

# 4 Conclusions

540

545

560

565

We use observations of aerosol (i.e. CCN) and cloud properties (i.e.  $N_d$ ) from airborne in-situ measurements taken during SOCRATES (the Southern Ocean Clouds, Radiation, Aerosol Transport Study, Figure 1) to constrain model parameters related to aerosol-cloud interactions. To systematically examine constraints on parameterized processes, we used a PPE that varies 45 parameters related to aerosol-cloud interactions. While a large number of ensemble members (i.e., 262) were integrated across 45-dimensional parameter space, this sampling was still very sparse in an absolute sense. To better map this space, we trained statistical emulators (Figure S2) to create a set of 1 million model variants. Each model variant was compared against observations and are retained if its implausibility is less than 1 based on the implausibility metric (Figure S3, Eq 4). Our constraint on processes in this framework (Figure 2, 3) resulted in a constraint on the anthropogenic perturbation to  $N_d$  ( $\Delta N_{d,PD-PI}$ ) (Figure 8).

Airborne observations of CCN and  $N_d$  over SOCRATES both constrain parameter spaces related to aerosol emission and precipitation processes (Figure 3), providing insights on developing in-situ instruments targeting these processes to better constrain cloud properties. Observations of  $N_d$  are more effective than CCN at constraining parameter space (Figure 3ab).

With constrained parameter space with observations of CCN and  $N_d$  (Section 3.2), we examine the likely range of  $\Delta N_{d,PD-PI}$  at the constrained parameter space. One key result is that observations of CCN alone have minimal constraint on  $\Delta N_{d,PD-PI}$ , but the constraint from observations of  $N_d$  is strong (Figure 8). This is sensible because aerosol concentrations from UH-SAS100 give information about the aerosol population, but they do not directly inform the activation of aerosols into droplets.

To explain why the constraints work when using observations of  $N_d$ , we use idealized sink-source models of  $N_d$  (Eq 11, 10). Previous work identifies the precipitation sink of droplets as a key driver of  $N_d$  variability (Kang et al., 2022; Wood et al., 2012; McCoy et al., 2020). We extended these budget models to anthropogenic perturbations to  $N_d$  (Figure 6), and used the result to understand relationships emergent from the CAM6 PPE (Figure 2, 4, 7). Within the  $N_d$  budget model framework, we

identified both the precipitation sink and how CCN form droplets as important in controlling the positive correlation between CCN and  $N_d$  (Figure 6bd), the positive correlation between present day (PD)  $N_d$  and  $\Delta N_{d,PD-PI}$  in CAM6 PPE (Figure 6ac).

Understanding the emergent behaviors from the CAM6 PPE (Figure 4), we next note that the amount of campaign-mean  $N_d$  over SOCRATES is a good approximate of the global oceanic-mean  $N_d$  (Figure 5). Within this framework, observations of  $N_d$  over SOCRATES constrains the amount of global  $\Delta N_{d,PD-PI}$  due to anthropogenic aerosol influence in the CAM6 PPE, with the strong positive correlation between PD  $N_d$  and  $\Delta N_{d,PD-PI}$  in CAM6 PPE (Figure 4), which can be explained in the context of  $N_d$  sources and sinks (Figure 6).

575

580

585

590

595

600

We find that the range of parameters associated with precipitation processes that are consistent with observations of CCN and  $N_d$  is narrow, suggesting the potential of using precipitation rate as an observational constraints on  $\Delta N_{d,PD-PI}$ . We examine what the constraints would be like if we know the observed surface precipitation. However, the constraints from two hypothetical surface precipitation is minimal (Figure S8). We did not include cloud base precipitation rate as a constraint due to the difficulty in comparing the simulated cloud base precipitation from CAM6 PPE with cloud base precipitation retrieved from cloud radar and lidar from SOCRATES. We identify further development of instrument simulators for global models as a useful avenue to improve our ability to leverage airborne data (e.g., cloud base precipitation) to constrain global behavior.

We find the constraints are sensitive to the implausibility setup. Overall, observations of  $N_d$  constrain  $\Delta N_{d,PD-PI}$  to a 12% reduction in range and a 16% increase in the median, under the condition of with emulator uncertainty (Figure 8a). The constraint is improved under condition of no emulator uncertainty, for which the reduction in range of  $\Delta N_{d,PD-PI}$  is 21% and the increase in the median is 28% (Figure 8b). The results suggest reducing emulator uncertainty is important for improving our constraint. More skillful emulators can be achieved by a careful selection of parameters focusing on key processes affecting ACI, particularly aerosol activation, cloud microphysics, and precipitation process as we discussed earlier in Section 3.2. Additionally, this work provides insights in the possible parameters ranges in creating PPEs in the discussion of parameter constraints in Section 3.

We examine the sensitivity of the constraints on  $\Delta N_{d,PD-PI}$  with observational uncertainties (Figure 9). We find discarding parameter combinations that don't mesh with observed CCN and  $N_d$  during SOCRATES yields an improved constraint on  $\Delta N_{d,PD-PI}$  when we disregard emulator uncertainty and when observational uncertainty decreases (Figure 9ab). This highlights the importance of considering systematic uncertainties in observations and continuing to develop our understanding of systematic uncertainty in observations of microphysics as well as designing campaigns that allow for stochastic sampling and more direct comparisons to ESMs.

In future work, incorporating additional in-situ constraints, such as aerosol composition, size distributions, or lidar–radarretrieved cloud and precipitation properties could further narrow the range of plausible PPE configurations. Alternatively,
adding more variables as observational constraints may expose structural model uncertainties if the observations are incompatible with any members of the PPE ensemble (Regayre et al., 2023). Instrument simulators that translate model outputs
into observation-like quantities (e.g., cloud-base precipitation rate) will also be essential for consistent comparisons. Moreover, incorporating variables such as ice-nucleating particles or ice crystal concentrations, could extend the PPE framework to
mixed-phase regimes. While such extensions are beyond the current scope of this study, which focuses on warm liquid clouds,

they represent promising directions for future work. Together, these directions can improve the use of PPEs in constraining aerosol-cloud interactions.

Code and data availability. The description of the PPE dataset is in Eidhammer et al. (2024). The PPE dataset used in this study is stored on the NCAR-Wyoming Super-computing Center for community access. The aerosol and cloud measurements from SOCRATES are available at https://data.eol.ucar.edu/dataset/552.002. Cloud droplet number concentration from MODIS is available at online in NetCDF format from the Centre for European Data Analysis (CEDA) (https://catalogue.ceda.ac.uk/uuid/cf97ccc802d348ec8a3b6f2995dfbbff/).

Author contributions. CS conducted the simulations of the PPE with configurations specific to this study with the help from TE and AG, conducted analysis of the data and wrote the manuscript. DTM initiated the idea of producing PPE simulations integrated along flight tracks, conducted analysis of the data and assisted in writing the manuscript. ILM contributed to the analysis of campaign observations and PPE outputs, provided input on the work and edited the manuscript. HB provided input on the manuscript and assisted in writing the manuscript. AG and TE assisted in running scripts for the PPE simulations and assisted in editing the manuscript. DB assisted in editing the manuscript.

Competing interests. The contact author has declared that none of the authors has any competing interests.

610

620

Acknowledgements. CS, DB, and DTM were supported by NASA Grant 80NSSC21K2014 and DTM was supported by the U.S. Department of Energy's Atmospheric System Research Federal Award DE-SC002227; U.S. Department of Energy's Established Program to Stimulate Competitive Research DE-SC0024161; U.S. Department of Energy's Earth and Environmental System Modeling DE-SC0025208; and NASA Precipitation Measurement Mission Science Team Grant 80NSSC22K0609. ILM was supported by the NOAA cooperative agreement NA22OAR4320151, for the Cooperative Institute for Earth System Research and Data Science (CIESRDS). The statements, findings, conclusions, and recommendations are those of the author(s) and do not necessarily reflect the views of NOAA or the U.S. Department of Commerce.

#### References

- Ackerman, A. S., Kirkpatrick, M. P., Stevens, D. E., and Toon, O. B.: The impact of humidity above stratiform clouds on indirect aerosol climate forcing, Nature, 432, 1014–1017, https://doi.org/10.1038/nature03174, 2004.
  - Bellouin, N., Quaas, J., Gryspeerdt, E., Kinne, S., Stier, P., Watson-Parris, D., Boucher, O., Carslaw, K. S., Christensen, M., Daniau, A.-L., et al.: Bounding global aerosol radiative forcing of climate change, Reviews of Geophysics, 58, e2019RG000660, 2020.
  - Bergeron, T.: On the physics of clouds and precipitation, Proc. 5th Assembly UGGI, Lisbon, Portugal, 1935, pp. 156–180, 1935.
- Bosilovich, M., Akella, S., Coy, L., Cullather, R., Draper, C., Gelaro, R., Kovach, R., Liu, Q., Molod, A., Norris, P., et al.: Technical report series on global modeling and data assimilation, volume 43 merra-2: Initial evaluation of the climate, NASA-GMAO. Retrieved from https://gmao.gsfc.nasa.gov/pubs/docs/Bosilovich803.pdf, 2015.
  - Carslaw, K., Lee, L., Reddington, C., Pringle, K., Rap, A., Forster, P., Mann, G., Spracklen, D., Woodhouse, M., Regayre, L., et al.: Large contribution of natural aerosols to uncertainty in indirect forcing, Nature, 503, 67–71, 2013.
- 635 Carslaw, K. S., Gordon, H., Hamilton, D. S., Johnson, J. S., Regayre, L. A., Yoshioka, M., and Pringle, K. J.: Aerosols in the pre-industrial atmosphere, Current Climate Change Reports, 3, 1–15, 2017.
  - Clarke, A. D., Owens, S. R., and Zhou, J.: An ultrafine sea-salt flux from breaking waves: Implications for cloud condensation nuclei in the remote marine atmosphere, Journal of Geophysical Research: Atmospheres, 111, 2006.
- Danabasoglu, G., Lamarque, J.-F., Bacmeister, J., Bailey, D., DuVivier, A., Edwards, J., Emmons, L., Fasullo, J., Garcia, R., Gettelman, A., et al.: The community earth system model version 2 (CESM2), Journal of Advances in Modeling Earth Systems, 12, e2019MS001916, 2020.
  - Eidhammer, T., Gettelman, A., Thayer-Calder, K., Watson-Parris, D., Elsaesser, G., Morrison, H., van Lier-Walqui, M., Song, C., and McCoy, D.: An extensible perturbed parameter ensemble (PPE) for the community atmosphere model version 6, EGUsphere, 2024, 1–27, 2024. Field, P. and Heymsfield, A.: Importance of snow to global precipitation, Geophysical Research Letters, 42, 9512–9520, 2015.
  - Field, P. R. and Furtado, K.: How biased is aircraft cloud sampling?, Journal of Atmospheric and Oceanic Technology, 33, 185–189, 2016.
  - Forster, P. M.: Inference of climate sensitivity from analysis of Earth's energy budget, Annual Review of Earth and Planetary Sciences, 44, 85–106, 2016.
  - Fossum, K. N., Ovadnevaite, J., Ceburnis, D., Dall'Osto, M., Marullo, S., Bellacicco, M., Simó, R., Liu, D., Flynn, M., Zuend, A., et al.: Summertime primary and secondary contributions to Southern Ocean cloud condensation nuclei, Scientific reports, 8, 13844, 2018.
- 650 Gettelman, A. and Morrison, H.: Advanced two-moment bulk microphysics for global models. Part I: Off-line tests and comparison with other schemes, Journal of Climate, 28, 1268–1287, 2015.
  - Gettelman, A., Morrison, H., Santos, S., Bogenschutz, P., and Caldwell, P.: Advanced two-moment bulk microphysics for global models. Part II: Global model solutions and aerosol–cloud interactions, Journal of Climate, 28, 1288–1307, 2015.
- Gettelman, A., Bardeen, C., McCluskey, C. S., Järvinen, E., Stith, J., Bretherton, C., McFarquhar, G., Twohy, C., D'Alessandro, J., and Wu, W.: Simulating observations of Southern Ocean clouds and implications for climate, Journal of Geophysical Research: Atmospheres, 125, e2020JD032 619, 2020.
  - Ghan, S., Wang, M., Zhang, S., Ferrachat, S., Gettelman, A., Griesfeller, J., Kipling, Z., Lohmann, U., Morrison, H., Neubauer, D., et al.: Challenges in constraining anthropogenic aerosol effects on cloud radiative forcing using present-day spatiotemporal variability, Proceedings of the National Academy of Sciences, 113, 5804–5811, 2016.

- 660 Grosvenor, D. and Wood, R.: The effect of solar zenith angle on MODIS cloud optical and microphysical retrievals within marine liquid water clouds, Atmospheric Chemistry and Physics, 14, 7291–7321, 2014.
  - Grosvenor, D. P., Sourdeval, O., Zuidema, P., Ackerman, A., Alexandrov, M. D., Bennartz, R., Boers, R., Cairns, B., Chiu, J. C., Christensen, M., et al.: Remote sensing of droplet number concentration in warm clouds: A review of the current state of knowledge and perspectives, Reviews of Geophysics, 56, 409–453, https://doi.org/10.1029/2017RG000593, 2018.
- 665 Gryspeerdt, E., Quaas, J., and Bellouin, N.: Constraining the aerosol influence on cloud fraction, Journal of Geophysical Research: Atmospheres, 121, 3566–3583, 2016.
  - Gryspeerdt, E., McCoy, D. T., Crosbie, E., Moore, R. H., Nott, G. J., Painemal, D., Small-Griswold, J., Sorooshian, A., and Ziemba, L.: The impact of sampling strategy on the cloud droplet number concentration estimated from satellite data, Atmospheric Measurement Techniques, 15, 3875–3892, 2022.
- 670 Hamilton, D. S., Lee, L. A., Pringle, K. J., Reddington, C. L., Spracklen, D. V., and Carslaw, K. S.: Occurrence of pristine aerosol environments on a polluted planet, Proceedings of the National Academy of Sciences, 111, 18466–18471, 2014.
  - Hudson, J. G. and Svensson, G.: Cloud microphysical relationships in California marine stratus, Journal of Applied Meteorology (1988-2005), pp. 2655–2666, 1995.
- Johnson, J. S., Regayre, L. A., Yoshioka, M., Pringle, K. J., Lee, L. A., Sexton, D. M., Rostron, J. W., Booth, B. B., and Carslaw, K. S.: The importance of comprehensive parameter sampling and multiple observations for robust constraint of aerosol radiative forcing, Atmospheric Chemistry and Physics, 18, 13 031–13 053, 2018.
  - Johnson, J. S., Regayre, L. A., Yoshioka, M., Pringle, K. J., Turnock, S. T., Browse, J., Sexton, D. M., Rostron, J. W., Schutgens, N. A., Partridge, D. G., et al.: Robust observational constraint of uncertain aerosol processes and emissions in a climate model and the effect on aerosol radiative forcing, Atmospheric Chemistry and Physics, 20, 9491–9524, 2020.
- Kang, L., Marchand, R., Wood, R., and McCoy, I. L.: Coalescence scavenging drives droplet number concentration in southern ocean low clouds, Geophysical Research Letters, 49, e2022GL097 819, 2022.
  - Kang, L., Marchand, R., and Wood, R.: Stratocumulus precipitation properties over the Southern Ocean observed from aircraft during the SOCRATES campaign, Journal of Geophysical Research: Atmospheres, 129, e2023JD039 831, 2024.
- Khairoutdinov, M. and Kogan, Y.: A new cloud physics parameterization in a large-eddy simulation model of marine stratocumulus, Monthly weather review, 128, 229–243, 2000.
  - King, M. D., Platnick, S., Menzel, W. P., Ackerman, S. A., and Hubanks, P. A.: Spatial and temporal distribution of clouds observed by MODIS onboard the Terra and Aqua satellites, IEEE transactions on geoscience and remote sensing, 51, 3826–3852, 2013.
  - Klein, S. A. and Hall, A.: Emergent constraints for cloud feedbacks, Current climate change reports, 1, 276–287, 2015.

690

695

- Lance, S., Brock, C., Rogers, D., and Gordon, J.: Water droplet calibration of the Cloud Droplet Probe (CDP) and in-flight performance in liquid, ice and mixed-phase clouds during ARCPAC, Atmospheric Measurement Techniques, 3, 1683–1706, 2010.
- Lee, L., Carslaw, K., Pringle, K., Mann, G., and Spracklen, D.: Emulation of a complex global aerosol model to quantify sensitivity to uncertain parameters, Atmospheric Chemistry and Physics, 11, 12 253–12 273, 2011.
- Mallet, M. D., Miljevic, B., Humphries, R. S., Mace, G. G., Alexander, S. P., Protat, A., Chambers, S., Cravigan, L., DeMott, P. J., Fiddes, S., et al.: Biological enhancement of cloud droplet concentrations observed off East Antarctica, npj Climate and Atmospheric Science, 8, 113, 2025.

- McCluskey, C. S., Gettelman, A., Bardeen, C. G., DeMott, P. J., Moore, K. A., Kreidenweis, S. M., Hill, T. C., Barry, K. R., Twohy, C. H., Toohey, D. W., et al.: Simulating Southern Ocean aerosol and ice nucleating particles in the Community Earth System Model version 2, Journal of Geophysical Research: Atmospheres, 128, e2022JD036 955, 2023.
- McCoy, D. T., Burrows, S. M., Wood, R., Grosvenor, D. P., Elliott, S. M., Ma, P.-L., Rasch, P. J., and Hartmann, D. L.: Natural aerosols explain seasonal and spatial patterns of Southern Ocean cloud albedo, Science advances, 1, e1500 157, 2015.
  - McCoy, D. T., Bender, F. A.-M., Grosvenor, D. P., Mohrmann, J. K., Hartmann, D. L., Wood, R., and Field, P. R.: Predicting decadal trends in cloud droplet number concentration using reanalysis and satellite data, Atmospheric Chemistry and Physics, 18, 2035–2047, 2018.
  - McCoy, I. L., McCoy, D. T., Wood, R., Regayre, L., Watson-Parris, D., Grosvenor, D. P., Mulcahy, J. P., Hu, Y., Bender, F. A.-M., Field, P. R., et al.: The hemispheric contrast in cloud microphysical properties constrains aerosol forcing, Proceedings of the National Academy of Sciences, 117, 18 998–19 006, 2020.

705

715

725

- McCoy, I. L., Bretherton, C. S., Wood, R., Twohy, C. H., Gettelman, A., Bardeen, C. G., and Toohey, D. W.: Influences of recent particle formation on Southern Ocean aerosol variability and low cloud properties, Journal of Geophysical Research: Atmospheres, 126, e2020JD033 529, 2021.
- McFarquhar, G. M., Bretherton, C. S., Marchand, R., Protat, A., DeMott, P. J., Alexander, S. P., Roberts, G. C., Twohy, C. H., Toohey,
  D., Siems, S., et al.: Observations of clouds, aerosols, precipitation, and surface radiation over the Southern Ocean: An overview of
  CAPRICORN, MARCUS, MICRE, and SOCRATES, Bulletin of the American Meteorological Society, 102, E894–E928, 2021.
  - Mohrmann, J., Wood, R., McGibbon, J., Eastman, R., and Luke, E.: Drivers of seasonal variability in marine boundary layer aerosol number concentration investigated using a steady state approach, Journal of Geophysical Research: Atmospheres, 123, 1097–1112, 2018.
  - Regayre, L. A., Johnson, J. S., Yoshioka, M., Pringle, K. J., Sexton, D. M., Booth, B. B., Lee, L. A., Bellouin, N., and Carslaw, K. S.: Aerosol and physical atmosphere model parameters are both important sources of uncertainty in aerosol ERF, Atmospheric Chemistry and Physics, 18, 9975–10006, 2018.
  - Regayre, L. A., Schmale, J., Johnson, J. S., Tatzelt, C., Baccarini, A., Henning, S., Yoshioka, M., Stratmann, F., Gysel-Beer, M., Grosvenor, D. P., et al.: The value of remote marine aerosol measurements for constraining radiative forcing uncertainty, Atmospheric Chemistry and Physics, 20, 10063–10072, 2020.
- Regayre, L. A., Deaconu, L., Grosvenor, D. P., Sexton, D. M., Symonds, C., Langton, T., Watson-Paris, D., Mulcahy, J. P., Pringle, K. J., Richardson, M., et al.: Identifying climate model structural inconsistencies allows for tight constraint of aerosol radiative forcing, Atmospheric Chemistry and Physics, 23, 8749–8768, 2023.
  - Schutgens, N., Dubovik, O., Hasekamp, O., Torres, O., Jethva, H., Leonard, P. J., Litvinov, P., Redemann, J., Shinozuka, Y., De Leeuw, G., et al.: AEROCOM/AEROSAT AAOT & SSA study, part I: evaluation and intercomparison of satellite measurements, Atmospheric Chemistry and Physics Discussions, 2020, 1–35, 2020.
  - Seinfeld, J. H. and Pandis, S. N.: Atmospheric chemistry and physics: from air pollution to climate change, John Wiley & Sons, 2016.
  - Silber, I., Jackson, R. C., Fridlind, A. M., Ackerman, A. S., Collis, S., Verlinde, J., and Ding, J.: The Earth Model Column Collaboratory (EMC 2) v1. 1: an open-source ground-based lidar and radar instrument simulator and subcolumn generator for large-scale models, Geoscientific Model Development, 15, 901–927, 2022.
- Song, C., McCoy, D. T., Eidhammer, T., Gettelman, A., McCoy, I. L., Watson-Parris, D., Wall, C. J., Elsaesser, G., and Wood, R.: Buffering of aerosol-cloud adjustments by coupling between radiative susceptibility and precipitation efficiency, Geophysical Research Letters, 51, e2024GL108 663, 2024.
  - Twomey, S.: The influence of pollution on the shortwave albedo of clouds, Journal of the atmospheric sciences, 34, 1149–1152, 1977.

- Wall, C. J., Norris, J. R., Possner, A., McCoy, D. T., McCoy, I. L., and Lutsko, N. J.: Assessing effective radiative forcing from aerosol–cloud interactions over the global ocean, Proceedings of the National Academy of Sciences, 119, e2210481 119, 2022.
  - Watson-Parris, D. and Smith, C. J.: Large uncertainty in future warming due to aerosol forcing, Nature Climate Change, 12, 1111–1113, 2022.
  - Watson-Parris, D., Williams, A., Deaconu, L., and Stier, P.: Model calibration using ESEm v1. 1.0–an open, scalable Earth system emulator, Geoscientific Model Development, 14, 7659–7672, 2021.
- Williamson, D., Goldstein, M., Allison, L., Blaker, A., Challenor, P., Jackson, L., and Yamazaki, K.: History matching for exploring and reducing climate model parameter space using observations and a large perturbed physics ensemble, Climate dynamics, 41, 1703–1729, 2013.
  - Wood, R.: Rate of loss of cloud droplets by coalescence in warm clouds, Journal of Geophysical Research: Atmospheres, 111, 2006.
  - Wood, R.: Stratocumulus clouds, Monthly Weather Review, 140, 2373–2423, 2012.
- Wood, R., Leon, D., Lebsock, M., Snider, J., and Clarke, A. D.: Precipitation driving of droplet concentration variability in marine low clouds, Journal of Geophysical Research: Atmospheres, 117, 2012.
  - Zhang, Z., Werner, F., Cho, H.-M., Wind, G., Platnick, S., Ackerman, A., Di Girolamo, L., Marshak, A., and Meyer, K.: A framework based on 2-D Taylor expansion for quantifying the impacts of subpixel reflectance variance and covariance on cloud optical thickness and effective radius retrievals based on the bispectral method, Journal of Geophysical Research: Atmospheres, 121, 7007–7025, 2016.
- Zheng, G., Wang, Y., Aiken, A. C., Gallo, F., Jensen, M. P., Kollias, P., Kuang, C., Luke, E., Springston, S., Uin, J., et al.: Marine boundary layer aerosol in the eastern North Atlantic: seasonal variations and key controlling processes, Atmospheric Chemistry and Physics, 18, 17615–17635, 2018.
  - Zheng, X., Dong, X., Xi, B., Logan, T., and Wang, Y.: Distinctive aerosol–cloud–precipitation interactions in marine boundary layer clouds from the ACE-ENA and SOCRATES aircraft field campaigns, Atmospheric Chemistry and Physics, 24, 10 323–10 347, 2024.
- 755 Zhou, X., Atlas, R., McCoy, I. L., Bretherton, C. S., Bardeen, C., Gettelman, A., Lin, P., and Ming, Y.: Evaluation of cloud and precipitation simulations in CAM6 and AM4 using observations over the Southern Ocean, Earth and Space Science, 8, e2020EA001 241, 2021.